



David Grafinger, BSc

Towards Ultraviolet Light Metaoptics

MASTER'S THESIS

to achieve the university degree of $\label{eq:Diplom-Ingenieur}$ Master's degree programme: Advanced Materials Science

submitted to

Graz University of Technology

Supervisor

Ass.Prof. Marcus Ossiander Institute of Experimental Physics

Abstract

Metalenses are two-dimensional nanophotonic devices that employ subwavelength structures to manipulate light in a precise and versatile manner. While these compact devices have already established a prominent role in the visible spectrum, the ultraviolet range remains dominated by conventional optics, which rely on scarce and expensive materials that involve complex processing. Propelled by recent advances in nanofabrication, the burgeoning field of ultraviolet metaoptics emerges as an excellent alternative to these traditional solutions. This thesis provides a comprehensive review of recent benchmarks in the field and, by careful selection of the candidate dielectric aluminum nitride, demonstrates the design of a propagation-phase-based ultraviolet metalens. On-axis focusing and off-axis redirection have been assessed at numerical apertures of 0.1 and 0.5, respectively, resulting in outstanding efficiencies of up to 65% at the selected wavelength of 351 nm. Atomic layer deposition was identified as the optimal fabrication route, and the production of a functional aluminum nitride metalens was initiated by the rigorous optimization of electron beam lithography-based templates. Furthermore, a resist-only metalens for the representative visible wavelength of 633 nm was designed, fabricated, and characterized. Its functionality serves as proof for the achieved precision and fabrication fidelity of the templates. The insights presented in this thesis serve as a foundation for further research on aluminum nitride metalenses, thereby contributing to the growing body of knowledge in ultraviolet metaoptics.

Kurzfassung

Metalinsen stellen eine spezielle Form planarer nanophotonischer Optiken dar, welche Strukturen im Subwellenlängenbereich nutzen, um Licht mit hoher Präzision und Flexibilität zu manipulieren. Während diese kompakten Metaoptiken im sichtbaren Spektrum bereits an Bedeutung gewonnen haben, werden Anwendungen für ultraviolettes Licht nach wie vor von kompromissbehafteten Optiken (Beugungslinsen, etc.) dominiert. Die jüngsten Fortschritte in der Nanofabrikation ebnen nun den Weg für Ultraviolett-Metaoptik, welche eine aussichtsreiche Alternative zu den bisherigen Lösungen darstellt. Diese Arbeit bietet einen umfassenden Überblick über die aktuellen Entwicklungen auf diesem Gebiet und demonstriert durch die sorgfältige Auswahl des Dielektrikums Aluminiumnitrid den Entwurf einer Ultraviolett-Metalinse, deren zugrundeliegende Interaktion auf dem Konzept der Propagationsphase basiert. Das Verhalten der Metalinse entlang der optischen Achse sowie bei Ablenkung von dieser Achse wurde bei numerischen Aperturen von 0,1 bzw. 0,5 evaluiert. Bei einer gewählten Wellenlänge von 351 nm ergab die entsprechende Datenauswertung herausragende Effizienzen von bis zu 65%. In weiterer Folge wurde Atomlagenabscheidung als optimaler Herstellungsweg identifiziert. Basierend darauf konnte die Herstellung der entworfenen Aluminiumnitrid-Metalinse durch die Optimierung von auf Elektronenstrahllithographie basierenden Fotolack- Negativschablonen in die Wege geleitet werden. Des Weiteren wurde eine Fotolack-Metalinse für eine Wellenlänge von 633 nm entworfen, hergestellt und charakterisiert. Ihre Funktionstüchtigkeit belegt die erreichte Herstellungspräzision der Negativschablonen. Die in dieser Arbeit präsentierten Erkenntnisse dienen als Grundlage für zukünftige Forschung an Aluminiumnitrid-Metalinsen und ebnen den Weg für weitere Innovationen in diesem Bereich.

Acknowledgements

I would like to express my gratitude to the following individuals and institutions for their support and collaboration throughout my research:

Firstly, I want to thank Joachim Krenn and Andreas Hohenau from the Institute of Physics at the University of Graz for providing access to the electron beam lithography system. Their collaboration and know-how was crucial for the success of this project. I am also grateful to Peter Hadley from the Solid State Physics Institute at Graz University of Technology for providing a profilometer, which tremendously simplified the preparatory work at the beginning of my thesis. Special thanks go to Anna Karner, whose expertise and assistance in countless lithography session were immensely helpful. Lastly, I extend my appreciation to my supervisor, Marcus Ossiander, for his continuous guidance and immediate support throughout my research.

Contents

T	Intro	oduction 1
	1.1	Classification of UV Radiation
	1.2	Important Applications and Benefits of UV Radiation
	1.3	Material and Optics Scarcity
	1.4	Chances of Metalenses for UV Radiation
	1.5	Thesis Outline
_	_	_
2		ndations 5
	2.1	What is a Metalens?
	2.2	Wavefront engineering
		2.2.1 The Meta-Atom
		2.2.2 The Phase Profile
	2.3	Metalens Design and Efficiency
3	Mat	erials for UV Metalenses 13
•	3.1	Material Review
	3.2	Selected Materials
4		nputational Approach to Metalenses 17
	4.1	Computational Methodology
	4.2	Computed Phase Maps
	4.3	Analysis of Simulated Metalenses
		4.3.1 Low-Aperture Lens
		4.3.2 High-Aperture Lens
		4.3.3 Discussion
5	Eab	rication 29
J	5.1	Electron Beam Lithography
	$5.1 \\ 5.2$	Preparatory Work
	0.2	5.2.1 Electron Beam Resist Spin Coating
		5.2.2 Data Preparation
	5.3	Fabrication Methodology
	0.0	5.3.1 Dose Test
		5.3.2 Proximity Correction
	5.4	Fabrication Results
	0.4	radication results
6	Pro	of of Concept - Resist Metalens 41
	6.1	Design and Simulation

	5.2 Fabrication 4 5.3 Characterization 4	
7	Discussion and Conclusion	51
8	Future Perspectives 5	53

List of Figures

1.1	Classification of ultraviolet radiation	1
2.1 2.2	Schematic representation of a fully illuminated metalens	5
	tion and refraction	6
2.3	Visualization of the the instantaneous electric field within two infinite waveguides exhibiting the same refractive index but different widths	8
2.4	Visualization and results of a meta-atom design	9
$\frac{2.5}{2.6}$	Exemplary phase profile of a metalens wrapped modulo 2π Two-dimensional schematic of a classical blazed grating and a construction	10
	of the wavefront emanating from a corresponding metasurface	11
2.7	Schematic representation of a metalens design workflow	11
2.8	Exemplary two-dimensional array of meta-atoms realizing a focusing phase	
	profile	12
3.1	Dispersion of the refractive index n and the extinction coefficient κ at the	10
2.0	electronic resonance in TiO_2	13
3.2	Dispersion of the refractive index for selected wide-bandgap dielectrics and semiconductors	15
3.3	Refractive index and extinction coefficient of AlN in the deep-UV to visible	10
0.0	regime	16
4.1	Visualization of the three-dimensional FDTD computational cell used to retrieve the phase map.	18
4.2	Resulting phase map and transmission of cylindrical AlN meta-atoms at	10
	various heights	19
4.3	Final phase map and transmission of cylindrical AlN meta-atoms	20
4.4	Simulated linear intensity profile of an AlN metalens with a numerical	
	aperture of 0.1	22
4.5	Simulated logarithmic intensity profile of an AlN metalens with a numer-	
	ical aperture of 0.1	23
4.6	Simulated logarithmic intensity profile of an AlN blazed grating with a	
	deflection angle of $\theta = 5.7^{\circ}$	23
4.7	Simulated logarithmic intensity profile of an AlN metalens with a numer-	
	ical aperture of 0.5	24
4.8	Simulated logarithmic intensity profile of an AlN blazed grating with a	
4.0	deflection angle of $\theta = 26.6^{\circ}$	25
4.9	2D layouts of all simulated metasurfaces	26

4.10	Cross-section of the initial Gaussian intensity distribution within the simulation cell	26
5.1	Schematic representation of the fabrication steps involved in the realization of AlN metalens designs	29
5.2	Visualization of a 100 µm diameter metalens layout across different magnifications	30
5.3	Measured and fitted spin curve of the electron beam resist AR-P 6200.13 (CSAR 62)	32
5.4	Workflow diagram of the ALD template fabrication process	33
5.5	Test series on electron beam resist CSAR 62 across multiple exposure doses for ALD templates	34
5.6	Schematic representation of the cross-sectional area that is influenced by proximity effects from forward and backscattered electrons	35
5.7	Exemplary energy deposition of an electron beam inside the resist	36
5.8	Comparison of an ALD template with and without proximity effect correction.	37
5.9	SEM images of all fabricated ALD templates	38
5.10	Detailed SEM images of all fabricated ALD templates	39
5.10 5.11		3 9
9.11	plate	39
6.1	Conceptional inversion from AlN template to resist-only metalens design.	42
6.2	Top view and hole diameter limit for resist-only metalens design	42
6.3	Resulting phase map and transmission of resist-only meta-atoms	43
6.4	Visualization of the resist-only metalens phase map	44
6.5	Simulated linear intensity profile of a resist-only metalens with a numerical aperture of 0.25	45
6.6	Simulated logarithmic intensity profile of a resist-only metalens with a	40
0.0	numerical aperture of 0.25	45
6.7	Test series on electron beam resist CSAR 62 across multiple exposure	40
0.1	doses for resist-only metalens	46
6.8	SEM images of fabricated resist-only metalens, superimposed with the	
	targeted GDSII layout	47
6.9	Schematic representation of the experimental setup used to characterize	4 -
0.10	the beam profile of the resist-only metalens	47
0.10	Intensity profile of the fabricated resist-only metalens with a numerical aperture of 0.1	48
	ADELLITE OF U.T.	40

List of Tables

3.1	Overview of UV metalens dielectrics, bandgaps, theoretical wavelength limits and possible fabrication methods	14
5.1	Excerpt on the system-specific ASCII file format from the software manual of the EBL system eLine Plus from Raith	32
6.1	List of optical components used in the experimental setup of Fig. 6.9. $$	47
7.1	Overview of hitherto achieved maximum focusing efficiencies of manufacturable UV spectrum metalenses	51

List of Acronyms

ALD atomic layer deposition.

CD critical distance.

EBL electron beam lithography.

EUV extreme ultraviolet.

FDTD finite-difference time-domain.

IC integrated circuits.

NA numerical aperture.

PECVD plasma-enhanced chemical vapor deposition.

PER particle-embedded resin.

PML perfectly matched layers.

RIE reactive ion etching.

SEM secondary electron microscope.

TO thermal oxidation.

UV Ultraviolet.

1 Introduction

The manipulation of light at the nanoscale, enabled by advancements in nanofabrication, has emerged as an innovative and flexible approach in UV optics. Prior to examining the specifics and potential of these so-called metaoptics, this introduction will define the spectral regime of interest, elucidate the inherent complexities of UV radiation, and explore the opportunities that metalenses offer in this domain. Finally, the outline of this thesis will provide a roadmap for the subsequent chapters.

1.1 Classification of UV Radiation

The term ultra is derived from Latin and signifies beyond something. In accordance with this definition, ultraviolet (UV) radiation is a form of light that extends beyond the last visibly discernible color, violet. As the wavelength decreases, increasing photon energies interact more strongly with electrons in wide-bandgap semiconductors and dielectrics, which is a prerequisite for various fields of research and applications (Sect. 1.2). The classification of UV radiation depends on the specific research field and context in question. Concerning medical investigations, the most prevalent classification is based on a standard set forth by the World Health Organisation in 1994 [1]. Therein, UV refers to wavelengths between 100 and 400 nm and is further divided into three subgroups: UV-A (315–400 nm), UV-B (280–315 nm) and UV-C (100–280 nm). In this context, the aforementioned subgroups account for different carcinogenic effects and, consequently, the impact on human health. From a physical perspective, the primary focus is shifted to matter-wave interactions, which necessitates a different classification. Figure 1.1 illustrates a subdivision of the UV spectrum that more closely aligns with these interests. In the context of this thesis, the targeted spectrum is that of near- to deep-UV wavelengths (190-380 nm). As the name implies, vacuum-UV light (and beyond) can only propagate in vacuum, as all matter becomes opaque. This renders classical optics, as well as the herein presented approach of metalenses, inapplicable. Notwithstanding that, concepts extending into the realm of EUV light have been proposed [2].



Figure 1.1: Classification of ultraviolet radiation as suggested by [3].

1.2 Important Applications and Benefits of UV Radiation

In the last decades, the ongoing miniaturization of integrated circuits (IC) continuously pushed the limits of technology and opened the door to unprecedented computational performance. From the beginning, optical lithography has played a crucial role in the quest for enhanced resolution [4]. The process described involves the use of light to transfer a geometric pattern from a template onto a photosensitive layer on a substrate. The center of attention in this process then and now is the achievable resolution or critical distance (CD) [5]:

$$CD = k_1 \frac{\lambda}{NA} \tag{1.1}$$

The numerical aperture NA is a system-dependent factor that describes the range of accepted/emitted angles. k_1 can be interpreted as the quality of the involved processes and typically ranges from 0.5 (Abbe limit) to 0.8 [6]. The most flexible variable in Eq. 1.1 is the wavelength λ . As a result, the most significant progress in the reduction of CD have included the development of new UV technologies like KrF (248 nm), as well as F₂-excimer (157 nm) lasers [7]. More recently, advances have been made into the EUV spectrum ($\lambda \approx 13.5$ nm), reducing the CD to below 10 nm [8].

Nevertheless, lithography is not the sole scientific domain that has benefited from advances to ever shorter wavelengths. As a famous example, attosecond metrology relies on ultrashort laser pulses to push the limits of time-resolved microscopy. As the name suggests attosecond short electromagnetic pulses are exploited to unlock the previously unaccessible time-domain of electron dynamics. The aforementioned ultrafast pump-probe experiments necessitate the utilization of coherent EUV radiation for the generation of these ultrashort pulses [9].

1.3 Material and Optics Scarcity

As elaborated, electromagnetic waves in the UV part of the spectrum (indicated in Fig. 1.1) have become indispensible in fundamental research as well as industrial applications with further examples ranging from quantum optics to the sterilization of medical equipment. In spite of this, optical elements for UV light are relatively scarce, complex and expensive. The following shall highlight the fundamental challenges and limitations that arise as the wavelength decreases.

Optical losses:

In order to manipulate an electromagnetic wave, it has to reflect off, transverse or penetrate a solid or gaseous material. Light-matter interactions within the material consequently result in absorption. Given that the extent of this absorption is, inter alia, inherently connected to the material's bandgap, it comes naturally that the response of the medium is energy dependent. As the photon energy increases it leaves the domain of rotational and vibrational resonances and enters the domain of (core) electronic energy levels. Accordingly, these interband transitions necessitate the use of ever wider

bandgap materials to avoid significant absorption. Past photon energies of 10 eV, the already meager selection of transparent materials completely diminishes. Consequently, vacuum-UV and EUV technology currently remains constrained to reflective and diffractive optics (multi-layer Bragg-reflectors, Fresnel zone plates, etc.) [5].

The preceding arguments lead to the conclusion that UV optical systems with sufficiently high photon energies necessitate the use of vacuum systems. At wavelengths below 200 nm, electronic resonances within the surrounding gas medium trigger increasing absorption, thus significantly restraining the usable optical path length.

Complex fabrication:

Beyond the previously outlined requirements for specific materials, fabrication demands escalate significantly across the UV spectrum. To illustrate, precision lenses are often classified by a maximum Peak-to-Valley error of $\lambda/8$. Consequently, if the wavelength used is halved, the Peak-to-Valley tolerances must be halved in order to maintain the same lens quality. An equivalent argument can be made about the layer thickness of multilayered structures, where the same absolute deviation leads to significantly more severe errors as the wavelength decreases. In addition to external tolerances, material purity becomes of increasing importance. As Rutherford scattering from sub-wavelength particles, such as inhomogeneities, scales with a factor of $1/\lambda^4$, even minimal imperfections cause severe attenuation [8].

Damage:

As dictated by the conservation of energy, photons will deposit their equivalent during an absorption process. Over time, this constant energy bombardment can lead to solarization, which worsens transmission properties. The argument of degradation also comes back to fabrication quality, as low-bandgap impurities will boost absorption and thus, long-term damage.

1.4 Chances of Metalenses for UV Radiation

Notwithstanding the inherent complexity of the UV spectrum, the domain is dominated by conventional optics. While applications for larger wavelengths benefit from a wide range of low-loss and high-index materials, the aforementioned constraints substantially limit the pool of applicable materials for near- to deep-UV light and even more so for vacuum-UV light and beyond. Accordingly, the bandwidth, function, procurement and producibility of such optics are adversely impacted.

While the fundamental challenges in manipulating UV light persist, the application of metaoptics offers significant potential for advancements in this area. Instead of relying on bulk refraction or reflection, these two-dimensional devices replicate this behavior with the collective interaction of their nanoscale structures with the incident wave. Compared to their conventional counterparts, through meticulous design, these devices can achieve enhanced performance as well as innovative, versatile, and flexible functions,

all within a low-loss, compact form factor. Enhanced performance includes features such as achromaticity, polarization-dependent light shaping, and tunable focal length, among others. Moreover, their small size is advantageous given the recent trend toward chip-scale applications, including imaging, displaying, and metrology. [10]

1.5 Thesis Outline

The objective of this thesis is to explore and expand the nascent field of UV metaoptics by designing a UV metalens from a novel material. Therein the thesis is structured in a way that provides a detailed account of each phase of the project, as outlined below. First, we conducted a comprehensive literature review and identified aluminum nitride (AlN) as the ideal candidate dielectric material, since it most effectively fulfills the requirements imposed by UV light.

Once AlN was selected, we initiated an extensive design and simulation process. Using finite-difference time-domain simulations, we evaluated the optical performance to identify the optimal UV metalens design.

The realization of this design involved the assembly of more than 10^6 nano-scale features, amassed in the perimeter of a submillimeter lens. The nanofabrication technique of atomic layer deposition (ALD) is renowned for its ability to deposit thin films with atomic-scale precision, making it ideal for constructing these intricate features. However, following this fabrication route necessitated the patterning of ALD templates. Consequently, we utilized electron beam lithography for the generation of a resist-based negative layout, which, in the context of this thesis, was optimized to meet the requisite accuracy for the ALD process.

As a proof of concept, we designed, simulated, and fabricated a functional resist-only metalens for the visible spectrum, based on the preceding methodology. We subsequently characterized the resulting metalens in a custom experimental setup to assess its focusing capabilities and overall performance, further validating the precision of the involved process steps.

2 Foundations

As indicated in the introduction, the sophisticated design of metasurfaces offers a potential solution to the fundamental complexity of UV light manipulation. The theoretical principles underlying these devices, along with the critical steps required to develop a functional metalens, will be examined in this chapter.

2.1 What is a Metalens?

Concerning the scientific context, the prefix "meta", derived from the Greek word meaning "beyond", signifies that the properties or capabilities of a meta-surface extend beyond those typically observed. These structures are generally composed of periodically arranged individual meta-atoms. Each of these unit cells exhibits sub-wavelength dimensions and fulfills a specific function based on its geometry and interaction mechanism. The collective effect of these individual microscopic manipulations, such as phase, amplitude, or polarization of the incident electromagnetic wave, is to shape, transform, or redirect the macroscopic beam. This concept is schematically illustrated in Fig. 2.1 for a metalens.

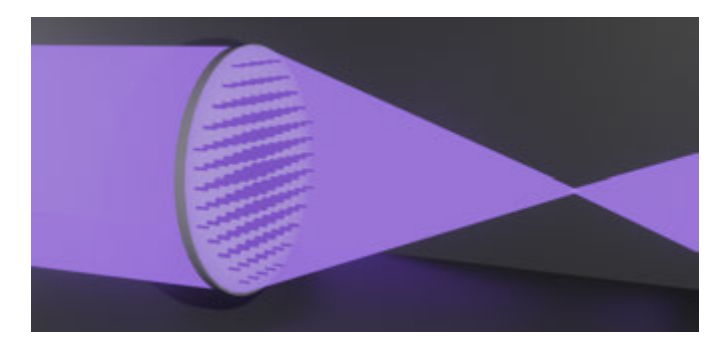


Figure 2.1: Schematic representation of a fully illuminated metalens.

The utilization of metasurfaces, however, extends beyond photonics and has attracted considerable interest over two decades in various scientific disciplines, including microfluidics and micromechanics [11]. Consequently, research in these fields has advanced considerably, leading to a vast number of applications and promising prospects. Despite this, the selection of meta-devices for UV light manipulation remains limited. This is especially true for the deep-UV to EUV spectrum. As this thesis aims to expand the selection of available meta-devices, it is essential to have a fundamental understanding of the working principles of metalenses. Accordingly, the subsequent sections will introduce wavefront engineering, with a particular emphasis on the utilization of metalenses.

2.2 Wavefront engineering

In contrast to conventional bulk optics, which exert a gradual phase shift on the wave along the propagation axis, the flat meta-counterpart has to achieve this phase modulation abruptly. Before elaborating on the mechanisms of interaction that define metalenses, it is necessary to establish a theory, that describes this phase discontinuity. Nanfang Yu et al. [12] revisited Fermat's principle, which asserts that light follows the path necessitating the least time for traversal. By considering a discontinuous phase with a transverse gradient $(d\phi/dx)$, they proposed a set of generalized laws of refraction (Eq. 2.1) and reflection (Eq. 2.2). Therein, n_1 and n_2 represent the refractive indices of the media. The incident, reflected and transmitted angles are denoted by θ_i , θ_r and θ_t , respectively. Finally, k_0 is the magnitude of the incident wave vector [12]:

Refraction:
$$n_2 k_0 \sin(\theta_t) - n_1 k_0 \sin(\theta_i) = \frac{d\phi(x)}{dx}$$
 (2.1)
Reflection: $n_1 k_0 \sin(\theta_r) - n_1 k_0 \sin(\theta_i) = \frac{d\phi(x)}{dx}$ (2.2)

Reflection:
$$n_1 k_0 \sin(\theta_r) - n_1 k_0 \sin(\theta_i) = \frac{d\phi(x)}{dx}$$
 (2.2)

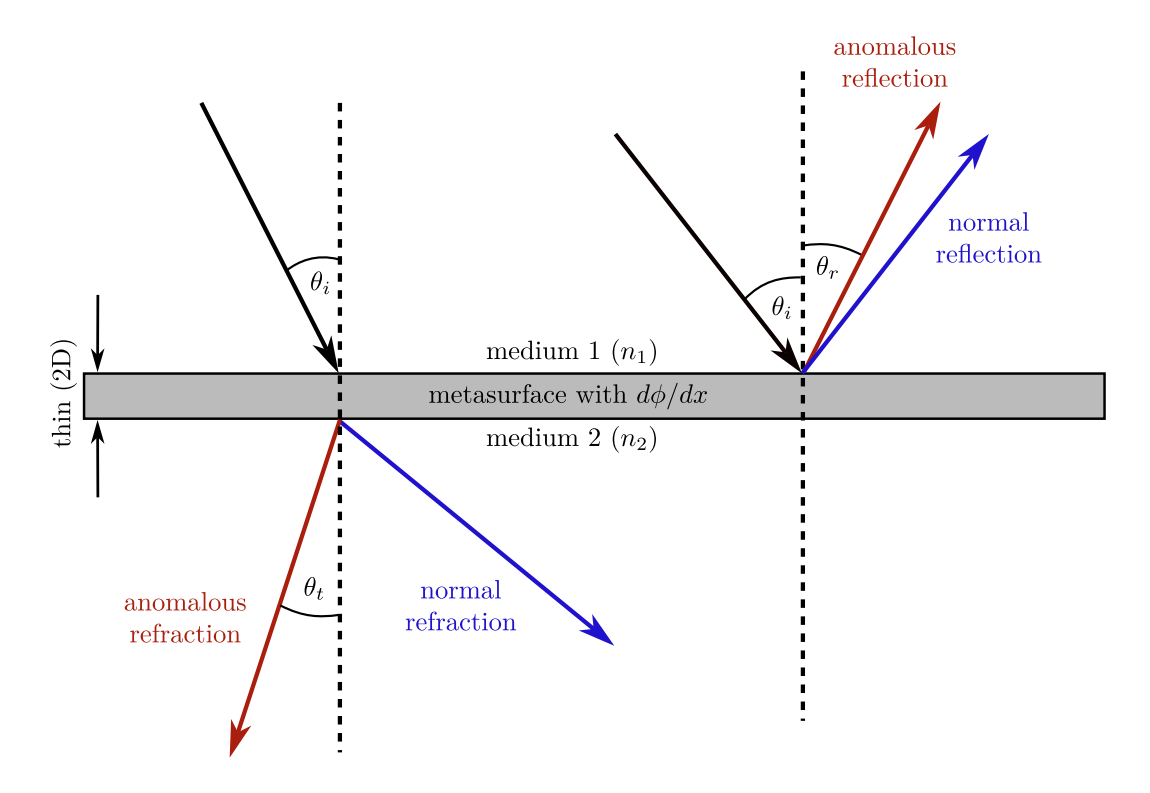


Figure 2.2: Schematic cross-sectional representation of the generalized law of reflection (right) and refraction (left).

By setting the phase gradient $d\phi/dx$ to zero, thus neglecting any discontinuities, one returns to the normal Snell's law, which is represented by the normal reflection and refraction trace in Fig. 2.2. Crucially, the presence of a controllable non-zero phase gradient (e.g. by a metasurface) implies a controllable reflection (θ_r) and refraction angle (θ_t) . Consequently, this enables the precise maneuverability of the anomalous traces depicted in Fig. 2.2, based on the collective interference of the individual phase-shifted elementary waves.

Continuing on this line of reasoning, the missing link to arbitrary wavefront engineering lies in the ability to implement arbitrary phase shifts within a two-dimensional array of meta-atoms. This concept will open the door to the intriguing multifunctionality of metalenses, which will surpass the limitations of conventional optical elements.

2.2.1 The Meta-Atom

Light-matter interaction within the meta-atom depends on the material, the individual meta-atom geometry, and the method of phase modulation. Said method can be categorized into three main types: resonant, geometric (or Pancharatnam-Berry) and propagation phase modulation [13]. The latter will be discussed in more detail. A general classification of meta-atoms can be made as follows [14]:

- Metals Plasmonic resonators: The free (surface) electrons of metallic metaatoms oscillate along an external electric field, resulting in the formation of surface electric dipoles. The resonance of these oscillations is dependent on the specific geometry and composition of the meta-atom. Modifying these parameters allows for the control of the meta-atom's oscillatory behavior, which can be exploited to modulate properties like phase, amplitude, or polarization of the incident wave.
- Dielectric resonators: The fundamental principle of wave modulation is analogous to that of plasmonic resonators: Shape and material of the dielectric metaatom determine the excitable modes of the oscillator. In contrast to the surface oscillations of plasmonic resonators, the source of the oscillatory behavior is the intense confinement of the electromagnetic wave inside the dielectric.
- **Dielectric waveguide:** High-index, sub-wavelength sized dielectric structures can function as microscopic waveguides and transversely confine the incident wave. In contrast to the concepts previously described, this approach eliminates the necessity of resonances, thereby facilitating broader transmission.

Concerning the final point, it is particularly important to note that the propagation behavior of the fundamental mode traversing the waveguide is contingent upon the transverse dimensions of the meta-atom. This is illustrated in Fig. 2.3, which shows a 2D simulation of two infinite waveguides made from materials with the same refractive index but different widths, both excited by light with the same vacuum wavelength. As can be seen, this difference results in a change in wave behavior. Assuming sufficient confinement, the change in phase velocity of the fundamental mode can be described by an effective refractive index $n_{\rm eff}$ of the meta-atom.

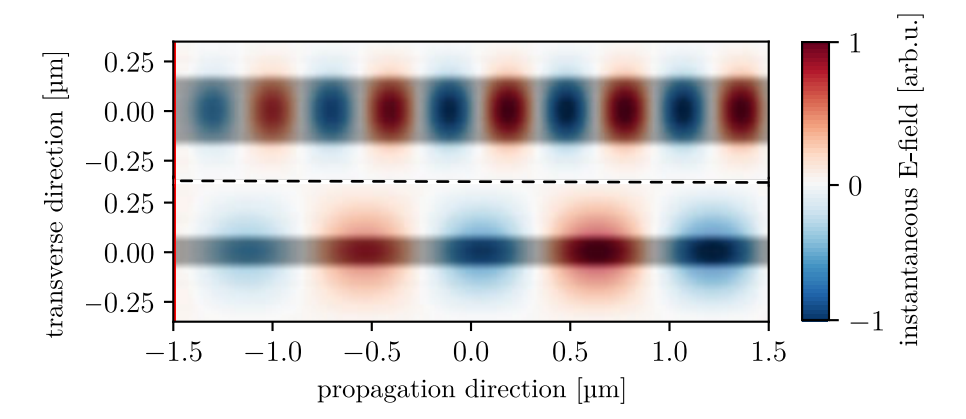


Figure 2.3: Visualization of the the instantaneous electric field within two infinite waveguides exhibiting the same refractive index but different widths.

Accordingly, the relative speed difference between two waves that travel through unequal adjacent waveguides is parameterized by the difference of relative effective indices $(\Delta n_{\rm eff} = n_{\rm eff,1} - n_{\rm eff,2})$. After traversing the full height h of the waveguide, said difference in phase velocity accumulated a local phase shift $\Delta \phi$ between the waves leaving the adjacent meta-atoms, as expressed in Eq. 2.3 [15]. Consequently, the careful control of each individual meta-atom shape (thus, $n_{\rm eff}$) collectively allows for arbitrary wavefront engineering (Eq. 2.1).

$$\Delta \phi = \frac{2\pi}{\lambda} \Delta n_{\text{eff}} h \tag{2.3}$$

There exist no analytical solutions for scattering from arbitrary shapes. Thus, in order to obtain the phase shift, numerical simulations such as finite-difference time-domain (FDTD, delineated in appendix) are utilized. By this computational approach, discrete particles of varying shape, as indicated in Fig. 2.4 (A,C), can successively be calculated. This offers the supplementary advantage of enabling the quantification of the transmission efficiency. Fig. 2.4 (B) depicts the results of such simulations, which are frequently referred to as phase libraries. As illustrated, an increase in diameter of the meta-atom (composed of a dielectric with an index n_1) results in a shift of the effective refractive index from n_2 (e.g. air) toward n_1 . This, in turn, leads to an increase in the phase delay relative to a phase reference.

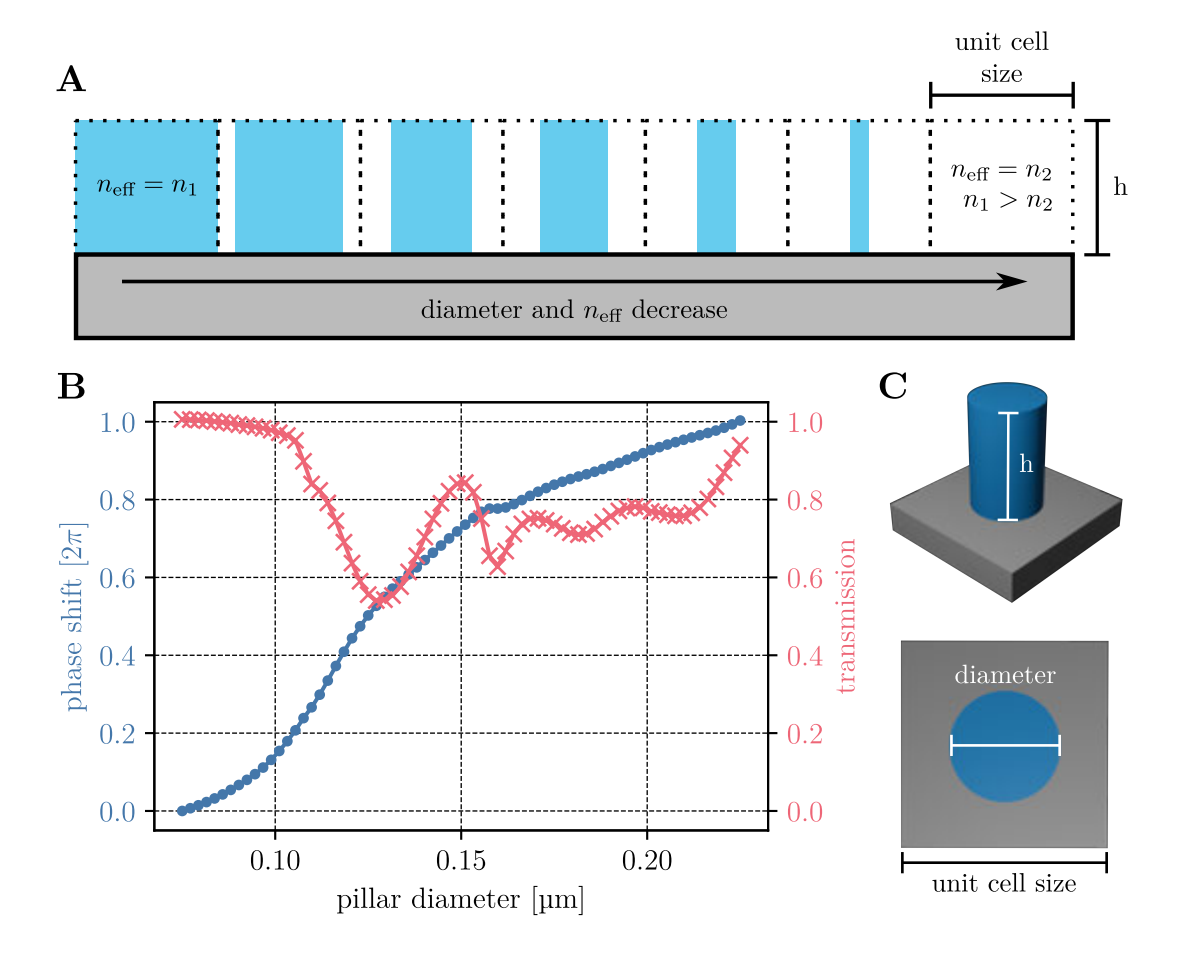


Figure 2.4: Visualization and results of a meta-atom design. (A) Schematic of the connection between meta-atom shape and effective refractive index $n_{\rm eff}$. (B) Resulting phase map and transmission efficiency of an exemplary meta-atom simulation. (C) 3D representation of a cylindrical meta-atom in a quadratic unit cell.

2.2.2 The Phase Profile

It is evident that using meta-atoms, the phase of a wave exiting the metalens can be modulated ad libitum. Consequently, the next step is to calculate a phase profile that fulfils a specific function and reproduce said profile using the meta-atoms. In the exemplary case of a lens, the objective is to focus a parallel beam into a focal point. The required phase discontinuity for said application is described by Eq. 2.4 [16]. The stated phase shift $\Delta \phi$ is derived from the Pythagorean theorem and induces constructive interference at the focal length f which is contingent upon the differential path length of waves that are emanated at a radial distance r from the optical axis.

$$\Delta\phi(r,\lambda) = -\frac{2\pi}{\lambda} \left(\sqrt{r^2 + f^2} - f \right) \tag{2.4}$$

Similar to the design of Fresnel lenses, the phase shift is kept small by wrapping Eq. 2.4 modulo 2π [17]. This is illustrated by Fig. 2.5. In the context of this thesis, the regions spanning a phase of 2π will henceforth be referred to as Fresnel zones.

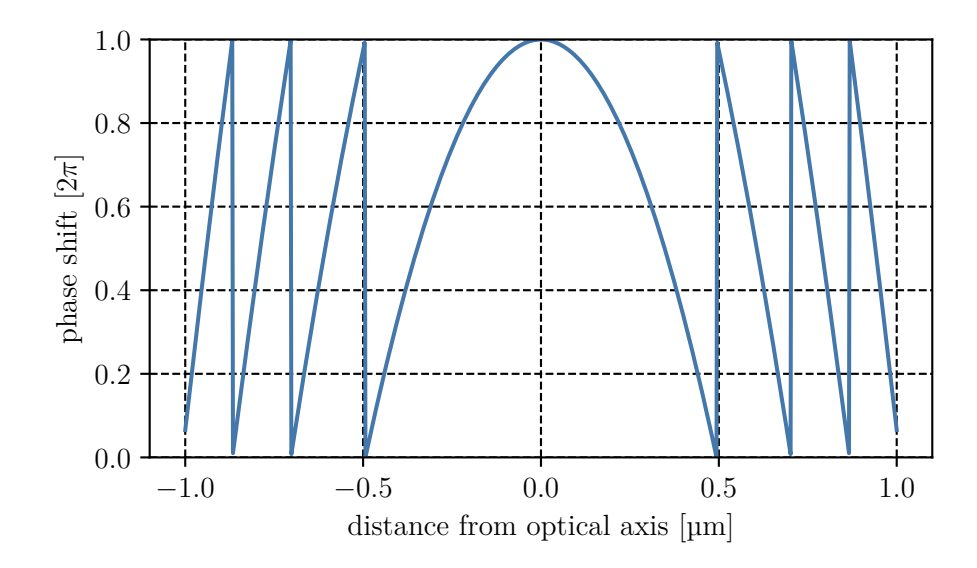


Figure 2.5: Exemplary phase profile of a metalens wrapped modulo 2π .

An equivalent concept can be applied to reproduce the behavior of blazed gratings (Fig. 2.6, left). They are a distinctive type of diffraction gratings that feature a sawtooth-like structure. Each sawtooth serves as a prism that redirects the beam into a specific grating order m, which is predetermined by the periodicity of the structure Δ_x . For a transmission grating at normal incidence, this relation reduces to Eq. 2.5. The underlying principle of this specific configuration is that the chosen diffraction order and refraction angle coincide, optimizing the grating efficiency at the blaze angle θ_b [18, p. 4].

$$m\lambda = \Delta_x \sin\left(\theta_b\right) \tag{2.5}$$

The translation of this concept into a metasurface necessitates knowledge about the phase profile of a blazed grating. As schematically depicted in Fig. 2.6 (right) the profile can be deduced by considering the angle of an outgoing wavefront that is propagating along the aforementioned diffraction order. The result of this construction can be seen in Eq. 2.6. Similar to the metalens design previously outlined, modeling the derived phase profile, wrapped modulo 2π , with the corresponding meta-atoms results in the formation of a meta-equivalent of a blazed grating.

$$\Delta \phi = kL = \frac{2\pi}{\lambda} x \sin(\theta_b) \tag{2.6}$$

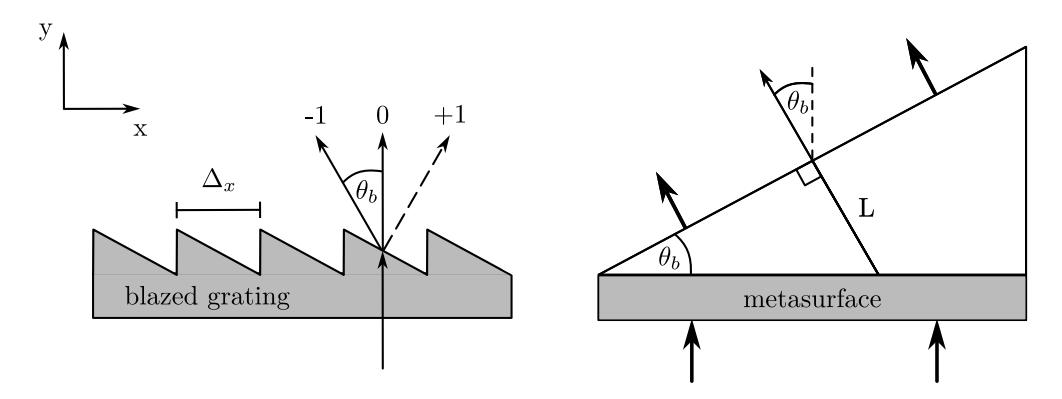


Figure 2.6: Two-dimensional schematic of a classical blazed grating (left) and construction of the requisite phase profile of a wavefront emanating from a corresponding metasurface (right).

2.3 Metalens Design and Efficiency

The design of a metalens can be divided into three steps, which are depicted schematically in Fig. 2.7. The first step is the choice and simulation of the meta-atom, which, as detailed in Sect. 2.2.1, facilitate a controllable phase shift and, moreover, allow for the incorporation of additional properties, such as polarization-dependent behavior. The second step is the selection and calculation of a phase profile, which dictates the spatially induced phase shift $\Delta \phi$ and, consequently, the shape of the emitted wavefront. Finally, the third step fuses both the continuous phase profile and the discrete discontinuity introduced by a specific meta-atom into the functional lens.

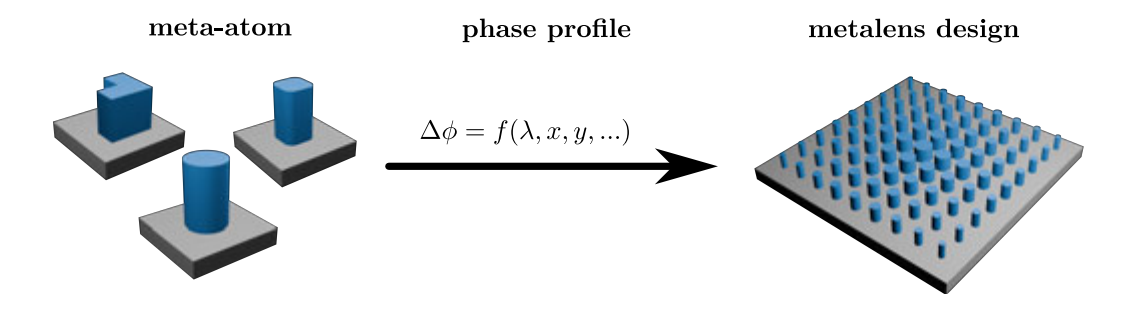


Figure 2.7: Schematic representation of a metalens design workflow.

With regard to this final step, the most straightforward approach is to discretize the phase profile on a Cartesian grid and place the meta-atoms corresponding to the locally required phase shift. An illustrative two-dimensional example of the resulting structure for a metalens with a phase profile governed by Eq. 2.4 is provided in Fig. 2.8.



Figure 2.8: Exemplary two-dimensional array of meta-atoms realizing a focusing phase profile.

While the transmission efficiencies of individual meta-atoms are defined in the phase library, the behavior of the final metalens is a more complex system, necessitating an evaluation of its collective behavior. Equation 2.7 attempts to describe the overall efficiency, denoted by the variable η , of this integrated system:

$$\eta = \frac{\text{correctly redirected beam power}}{\text{incident beam power}}$$
(2.7)

Of particular interest in this context are high-NA applications. As the distance from the optical axis increases, the lens must deflect the beam to a greater extent. This results in narrower Fresnel Zones (Fig. 2.5) and thus a steeper phase gradient within each zone. The subsequent discretization of this phase by the uniformly spaced meta-atoms reduces the phase sampling per Fresnel Zone with increasing distance from the optical axis, leading to a decrease in redirection efficiency. The overall performance of the lens can be understood as a superposition of these individual deflection efficiencies. Optical devices that permit a more rigorous analysis of this high-NA behavior are blazed gratings. They redirect the incident beam away from the optical axis, thereby separating it from light that traversed the metasurface without being affected, which is henceforth denoted as non-diffracted light [19].

3 Materials for UV Metalenses

As has been thoroughly discussed in Sect. 1.3, the selection of materials for UV applications is strongly reduced by the optical requirements. The criterion for suitable substrates is maximized transparency. On the other hand, suitable meta-atom materials are further limited by the necessity for high refractive indices coupled with minimal extinction coefficients. The following sections will provide an overview of available UV-compatible materials, their applicability to metalens fabrication, and a basic literature review.

3.1 Material Review

The previously stated circumstances are further evaluated using the example of TiO₂, which has, owing to its special refractive properties in the visible range, found frequent applications in metalens technology [20]. However, as indicated by the dispersion of the refractive index and extinction coefficient in Fig. 3.1, this advantageous regime terminates at near-UV wavelengths. While an increase in the refractive index is generally beneficial, the approaching electronic resonance also implies an undesirable increase in the extinction coefficient and thus in absorption.

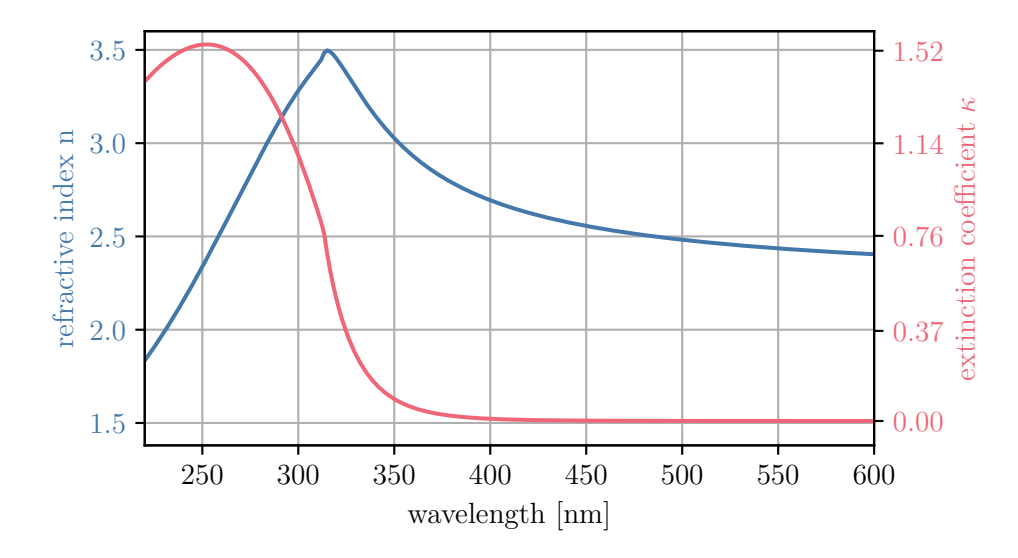


Figure 3.1: Dispersion of the refractive index n and the extinction coefficient κ at the electronic resonance in TiO₂ [21].

The preceding argument and Fig. 3.1 demonstrate that materials eligible for UV metalenses should exhibit an electronic resonance in proximity to the wavelength of interest to ensure a sufficient refractive index while simultaneously maintaining adequate spectral distance to limit absorption. This presupposes a sufficiently large bandgap. For example, to cover the deep-UV regime, a minimum band gap of 4.43 eV is required. Another factor is the feasibility of fabrication. Diamond $(E_g = 5.5 \,\mathrm{eV})$ and sapphire $(E_g = 8.8 \,\mathrm{eV})$ are examples of materials that fulfill the spectral requirements, although they lack easy processability. With regard to the bandgap, fluoride compounds have attracted a substantial amount of attention due to their ultra-wide energy gap of up to 14 eV [7]. This group of materials, exhibiting bandgaps that are already in the range of the ionization energy of hydrogen (13.6 eV) do, however, lack a sufficiently large refractive index that would allow for arbitrary wavefront engineering. Nevertheless, these fluoride compounds are promising candidates for UV-transparent metalens substrates and potential ultra-wide bandgap optoelectronic devices for UV applications [3]. In consideration of the aforementioned arguments, Tab. 3.1 provides an overview of widebandgap dielectrics and their possible fabrication processes. It is important to note that this list is not exhaustive but rather servers as a suggestion based on currently published scientific literature and the criteria of a bandgap exceeding 4.43 eV, as well as a refractive index larger than 1.5.

Table 3.1: Overview of UV metalens dielectrics, bandgaps, theoretical wavelength limits and possible fabrication methods.

material (composition)	E_g [eV]	$\lambda_{\min} [nm]$	possible fabrication processes
Hafnia (HfO ₂)	5.7	218	ALD [22]
Silica (SiO_2)	9.3	133	ALD [23], RIE and TO [24],
Aluminum Nitride (AlN)	6.0	207	ALD [25]
Silicon Nitride (Si_3N_4)	5.1	243	PECVD and RIE [26]
Magnesia (MgO)	7.8	159	RIE [27]
Zirconia (ZrO_2)	6.0	207	printable nano-PER [28]

Given that all dielectrics listed in Tab. 3.1 meet the criteria for UV metalenses, it is expectable that simulations and theoretical studies have already been conducted on each of them [3]. In contrast, experimental work on linear high-efficiency UV metalenses has, to our knowledge, only been conducted on hafnia [22], silicon nitride [26] and zirconia [28]. The brevity of this list is primarily due to the demanding fabrication process of the high-aspect-ratio meta-atoms. In the case of hafnia, the implementation of a novel low-temperature atomic layer deposition (ALD) allowed for a metalens design at 266 nm with 56% efficiency. Similarly, the development of fabrication processes for zirconia led to the creation of a printable nano-particle-embedded resin (nano-PER). This novel technique permitted the design of an unsurpassed UV metalens at 248 nm with 48% efficiency. In parallel, the combination of plasma-enhanced chemical vapor deposition (PECVD) with subsequent reactive ion etching (RIE) enabled bandgap engineering in

near-UV silicon nitride metalenses, expanding the energy gap to 5.9 eV [26].

Although the numerical predictions of the remaining materials of Tab. 3.1 are as promising as those of the aforementioned ones, functional realizations of UV metalenses have not yet materialized. This is despite the fact that potential fabrication processes exist, but have not yet been implemented for the design of an UV metalens. In the case of magnesia, high aspect ratio RIE of thin films has already been achieved, although additional steps are required due to the necessity for a hard mask [27]. By direct RIE of SiO₂ [29], as well as RIE of Si and subsequent thermal oxidation (TO) to SiO₂ [24], metalenses for the visible range have already been realized. The inevitable high aspect ratios resulting from the low UV index of refraction of SiO₂, however, limit the applicability of these approaches for decreasing wavelengths. Low-temperature ALD of SiO₂ has been successfully performed and could serve as an additional fabrication route [23], though the incorporation of hydrogen impurities at low deposition temperatures may potentially cause unwanted absorption. Ín addition to the potential metamaterial aspect, SiO₂ with its 9.3 eV bandgap also serves as an abundant UV-transparent substrate, similar to the previously mentioned fluorides.

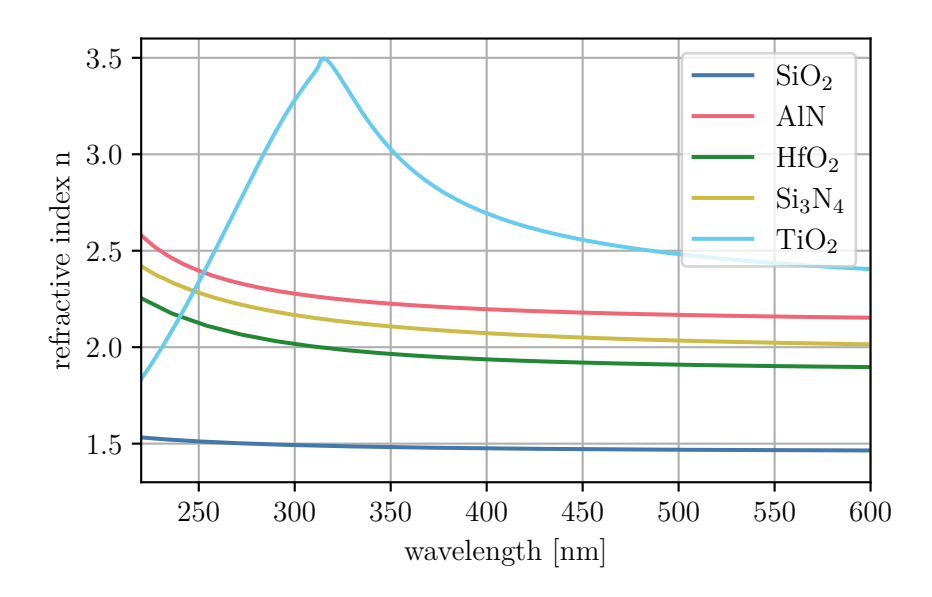


Figure 3.2: Dispersion of the refractive index of the wide-bandgap dielectrics and semi-conductors SiO_2 [30], AlN [31], HfO_2 [32] and Si_3N_4 [33], including TiO_2 [21] to indicate the approaching electronic resonances.

The final unmentioned material in Tab. 3.1, AlN, exhibits the highest refractive index across the near- to deep-UV spectrum. This is illustrated by Fig. 3.2. All therein plotted materials, with the exception of AlN, have been implemented in functional metalens realizations. TiO₂ was once again included to highlight the resonant behavior of all materials towards the vacuum-UV regime. ZrO₂ was excluded from Fig. 3.2 due to the weight-ratio-dependent refractive index of the nano-PER, which generally fluctuates between those of HfO₂ and SiO₂ [28]. With regard to the fabrication process of AlN

metalenses, low-temperature ALD has been demonstrated to grow films with low impurity and high optical performance, which is essential for the fabrication of high-efficiency UV applications [25].

3.2 Selected Materials

In consideration of UV-transparent substrates, abundant high-quality SiO_2 wafers outperform ultra-wide bandgap dielectrics. Thus, in the scope of this thesis, we selected UV-grade fused-silica wafers as the substrate.

Concerning the choice of material for the meta-atoms, those dielectrics that have already been the subject of experimental investigation exhibit few novel potential. Among the remaining wide-bandgap dielectrics, AlN occupies a distinctive position, exhibiting the largest refractive index (n>2) over the targeted UV regime. This characteristic allows for the broadest range of effective refractive indices, thereby relaxing the necessary form factors of individual meta-atoms. Concurrently, the materials' absorption remains minimal with $\kappa < 0.033$ down to 250 nm, as can be seen in Fig. 3.3 [31]. In light of these advantages, along with the promising fabrication approach of low-temperature ALD, we selected AlN for further investigation.

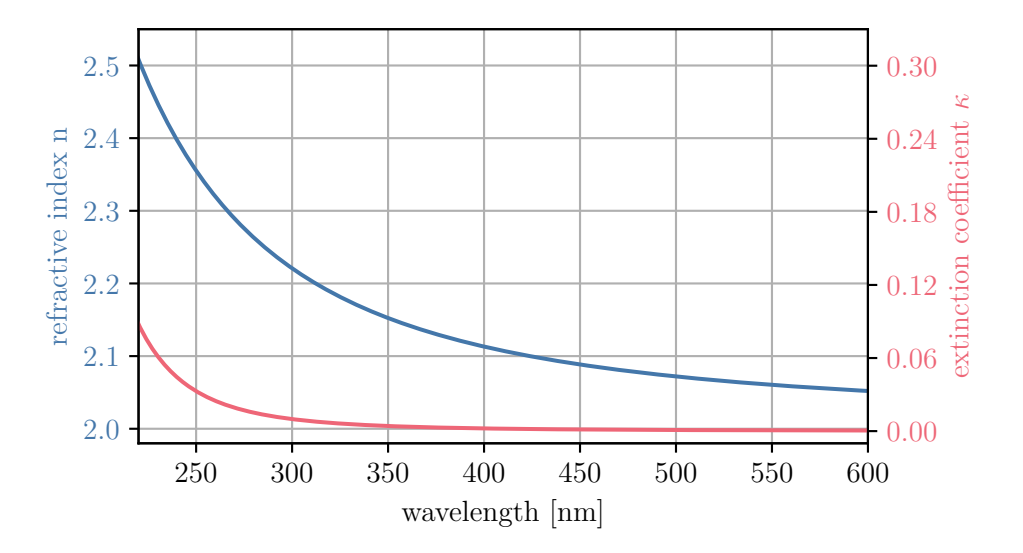


Figure 3.3: Refractive index and extinction coefficient of AlN in the deep-UV to visible regime [31].

4 Computational Approach to Metalenses

We design metalenses, following the concepts delineated in Sect. 2.3, by modeling metaatoms and full devices using FDTD simulations. The numerical implementation of this process is achieved with the open-source Python package MEEP. The subsequent sections will provide an overview of the methodology we employ to obtain the phase map, as well as a computational validation of the function of the final metalens design. The custom scripts necessary for this process were developed from the ground up during the context of this thesis.

4.1 Computational Methodology

The primary phase modulation principle we employed in this study was propagation phase via dielectric waveguide meta-atoms. As detailed in Sect. 2.2, this approach leverages the varying phase velocity of electromagnetic waves within high-index waveguides. These waveguides were designed as cylinders with varying diameters (varying $n_{\rm eff}$, Sect.2.2.1) and a constant height. We selected this rotationally symmetric design to minimize resolution-related errors during fabrication, such as rounded edges. The rationale behind constant height meta-atoms is solely related to fabrication issues, as a heterogeneous height would imply an immense increase in production complexity. In light of the aforementioned design considerations and the material selection, the strategy delineated in Sect. 2.3 was implemented. This entailed the retrieval of the employed phase shift of individual cylinders for varying diameters. In terms of FDTD simulations, this requires the definition of a three-dimensional computational cell that includes the geometry of interest, a radiation source, and a monitor at which the information of the phase-manipulated wave accumulates. Fig. 4.1 (top) depicts the two-dimensional cross-section of the three-dimensional cell containing one unit cell with a single metaatom on the substrate, as well as so-called perfectly matched layers (PML) at the minor faces of the three-dimensional rectangular cuboid cell. This special layer simulates open boundary conditions by absorbing all penetrating waves. Perpendicular to the direction of propagation (Fig. 4.1: y- and z-axis), Bloch-periodic boundary conditions were introduced to account for the periodic arrangement of meta-atoms in a device. This was subsequently exploited in a near-to-far-field transformation that considered a defined number of Bloch-periodic copies $(2n_{period} + 1)$ to retrieve the phase information of the emanating wavefront. The periodicity of this structure is illustrated by the schematic in Fig. 4.1 (bottom), where $n_{\text{period}} = 2$. When n_{period} is sufficiently large, the calculated far-field converges, allowing it to be mapped back to its influence in an array. By repeating this process for all relevant diameters, the desired phase map is obtained.

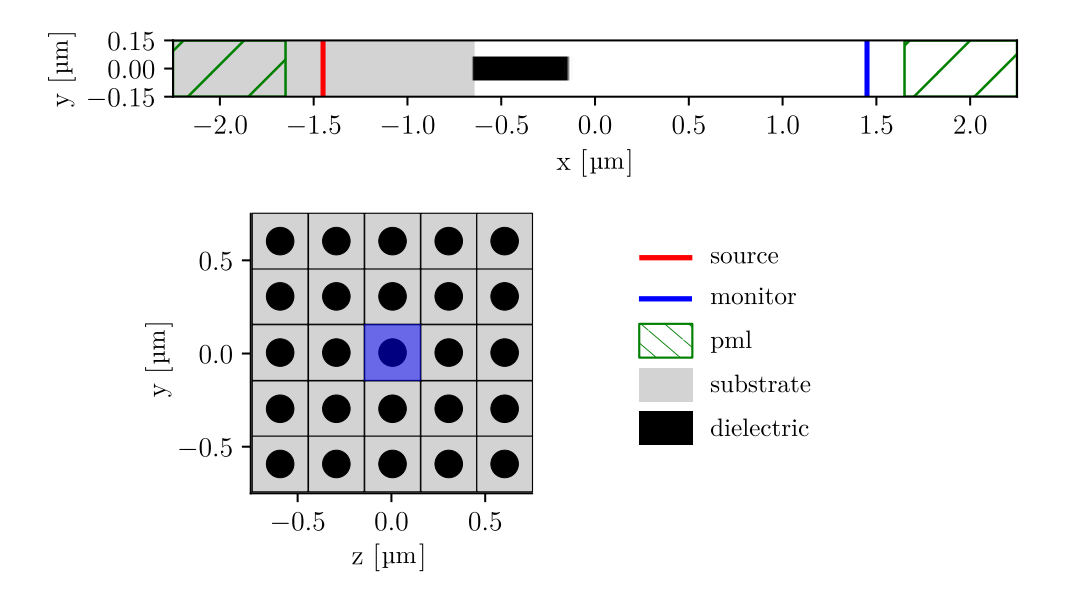


Figure 4.1: Visualization of the three-dimensional FDTD computational cell used to retrieve the phase map. Top: cross-section of the computational cell. Bottom: top view of exemplary Bloch-periodic boundary conditions with $n_{\text{period}} = 2$.

The final required element is the wavelength of interest which also determines the desired periodicity and meta-atom size. We chose 351 nm because a laser at this wavelength is accessible within our laboratory. For AlN, this corresponds to a refractive index and an extinction coefficient of n=2.15 and $\kappa=0.0041$, respectively [31]. Consequently, the wavelength inside the dielectric is at its minimum reduced to $\lambda=\lambda_{\rm vac}/n=163$ nm. This value would ideally serve as an upper limit for the unit cell size, thereby eliminating efficiency losses from scattering into low diffraction orders. However, the effective refractive index $n_{\rm eff}$ never attains the bulk value of $n_{\rm AlN}=2.15$, due to the cylindrical symmetry of individual meta-atoms in the Cartesian unit cell grid. $n_{\rm eff}$ can be approximated based on the volume ratio in Eq. 4.1. This yields a maximum value of $n_{\rm eff}\approx 1.9$ for a perfectly inscribed cylinder of the volume $V_{\rm AlN}$ in the rectangular cuboid unit cell of the volume $V_{\rm uc}$. Furthermore, a minimal feature distance and size reduce the fabrication complexity. This additional margin between adjacent cylinders further decreases the dielectric's volume fraction and thus $n_{\rm eff}$.

$$n_{\text{eff}} = \frac{V_{\text{air}} \cdot 1 + V_{\text{AlN}} \cdot n_{\text{AlN}}}{V_{\text{air}} + V_{\text{AlN}}} = \frac{(V_{\text{uc}} - V_{\text{AlN}}) \cdot 1 + V_{\text{AlN}} \cdot n_{\text{AlN}}}{V_{\text{uc}}}$$
(4.1)

In consideration of the aforementioned factors, we selected a unit cell dimension of 300 nm and a minimal feature size of 75 nm. Consequently, the pillar diameter ranged from 75 to 225 nm, resulting in an effective refractive index range of approximately 1.06 to 1.51 (Eq. 4.1).

4.2 Computed Phase Maps

As a next step, we calculated phase maps for the selected range of cylindrical metaatoms for varying pillar heights. The result of this series of tests, illustrated in Fig. 4.2, identifies the range of diameters required to achieve the desired phase coverage of 2π (Sect. 2.2.1), as well as regions of low transmission or strong resonance within the metaatoms. As anticipated, Fig. 4.2 reveals a greater phase shift for larger pillars, attributable to the increased propagation distance within the dielectric waveguide. At a height of $h = 400 \,\mathrm{nm}$ the desired shift of 2π is surpassed. Pillars deviating from this specific height exhibit significant losses, resulting in efficiencies as low as 5%. Conversely, at $h = 400 \,\mathrm{nm}$, transmission efficiencies remain consistently high, with a minimal value of 50%. Based on this observation, we selected this height.

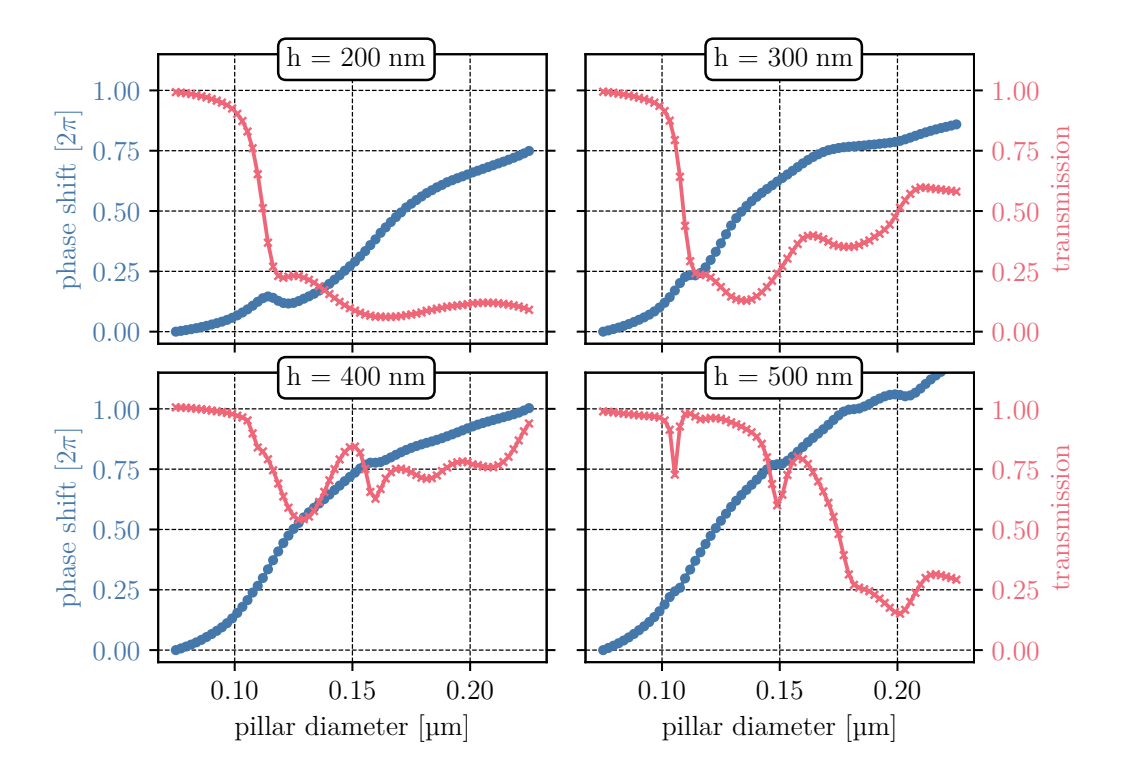


Figure 4.2: Resulting phase map and transmission of cylindrical AlN meta-atoms at various heights h with a unit cell size of 300 nm and a minimal feature size of 75 nm.

It should be noted that we generated the phase maps in Fig. 4.2 without including the imaginary component of the dielectric function, thus disregarding absorption losses. Although the extinction coefficient of AlN at 351 nm is low, its effect is still discernible in both the transmission efficiency and the phase shift, as seen in Fig. 4.3. In comparison to the purely real calculations depicted in Fig. 4.2, the total phase shift is slightly reduced, falling marginally below 2π . A comparable reduction can be observed in the transmission

minima, which exhibit a small shift towards larger diameters. Despite this influence, the computed phase map remains suitable for designing UV metalenses. The following list summarizes the most relevant simulation parameters used to generate Fig. 4.3:

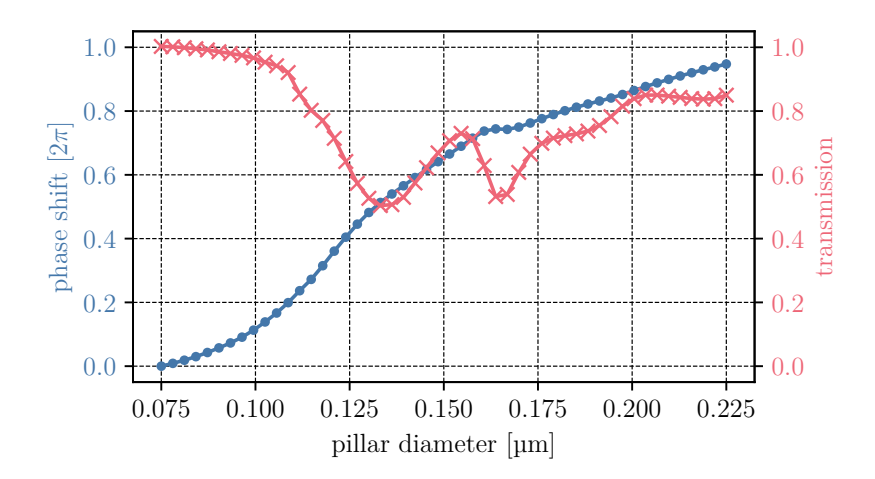


Figure 4.3: Final phase map and transmission of cylindrical AlN meta-atoms for $\lambda = 351\,\mathrm{nm}$ at a height of 400 nm, a unit cell size of 300 nm, and a minimal feature size of 75 nm.

4.3 Analysis of Simulated Metalenses

With the phase map of the AlN meta-atoms, we can now create metasurfaces with a multitude of phase profiles. For a more rigorous analysis, we chose two specific metalens variants, with numerical apertures (NA) of 0.1 and 0.5, for computational exploration and subsequent fabrication. The latter was realized in the form of GDSII layouts at a workable lens diameter of 100 μ m and will be detailed in Sect. 5.4. For a given lens design and refractive index n, Eq. 4.2 [34] links the focal length f, the lens diameter D, and the NA. It is obtained by geometric considerations about the right-angle triangle formed by D, f, and their included angle θ (opening half-angle of the lens).

$$NA = n \sin(\theta) = n \sin\left(\arctan\left(\frac{D}{2f}\right)\right)$$
 (4.2)

The specified NA also dictates the diffraction-limited waist $w_{d.l.}$ of the beam in the focal plane. In the paraxial approximation, the divergence angle θ , which is equivalent to

the opening half-angle θ in Eq. 4.2, can be expressed as shown in Eq. 4.3 [35, pp. 3.5-3.6]:

$$\theta = \arctan\left(\frac{D}{2f}\right) \approx \frac{D}{2f} = \frac{2\lambda}{\pi w_{d,l}}$$
 (4.3)

With regard to a numerical aperture of 0.5, this approximation is evidently approaching the limits of its validity. Nevertheless, the resulting deviations remain relatively minor. The rearrangement of the equation above allows for the estimation of the diffraction-limited waist $w_{d.l.}$ as defined in Eq. 4.4. In comparison to the measured focal spot size, this approximation can be employed to assess the quality of the designed metalens.

$$w_{d.l.} \approx \frac{4\lambda f}{\pi D}$$
 (4.4)

One unit cell $(0.3x0.3x3\,\mu\text{m})$ can easily be numerically modeled on a personal computer. However, implementing a reasonably sized metalens necessitates substantially more memory and computational time. Consequently, we restricted the dimensions of all designs to a maximum cross-sectional area of $30x30\,\mu\text{m}$ for full-lens simulations. In the propagation direction, the cell remained unaltered (see Fig. 4.1), and Bloch-periodic boundaries were substituted with PMLs. We then propagate the transmitted field into the far-field to extract the focusing properties. The efficiency of the design in redirecting waves (Eq. 2.7) was assessed both by directly analyzing the focal spot and by examining the maximum deflection angles. In particular, we engineered blazed gratings of the same NA as the metalenses to steer incoming waves towards these angles, effectively separating them from the unaffected radiation and thus providing a clearer measure for the redirection efficiency. The determination of the focal spot width was conducted in accordance with the ISO international standard method. Therein, the waist w is defined as 4σ , where σ is the second moment of the intensity profile I as a function of the radial distance r from the optical axis and specified by Eq. 4.5 [36].

$$w = 4\sigma = 4\sqrt{\frac{\int_{-\infty}^{\infty} I(r)(r-\bar{r})^2 dr}{\int_{-\infty}^{\infty} I(r) dr}} \text{ with } \bar{r} = \frac{\int_{-\infty}^{\infty} I(r) r dr}{\int_{-\infty}^{\infty} I(r) dr}$$
(4.5)

4.3.1 Low-Aperture Lens

We designed the first AlN UV metalens with a NA of 0.1. Given a Gaussian source diameter $(1/e^2)$ of 20 µm and the refractive index of air (n=1), a focal length of 100 µm was obtained with Eq. 4.2. By substituting this value into Eq. 2.4 and applying a modulo 2π operation, the desired phase profile was calculated. Subsequently, this profile was translated into the corresponding meta-atom diameters using Fig. 4.3 and incorporated into the FDTD simulation, generating the beam profile and corresponding focal plane in Fig. 4.4. According to the estimation in Eq. 4.4, an ideal diffraction-limited lens with the present design parameters would generate a focal spot size of $w_{d.l.} = 2.2 \,\mu\text{m}$. In comparison, the focal plane analysis of the simulated metalens, as indicated by Eq. 4.5, yielded a focal spot size of $w = 2.5 \,\mu\text{m}$.

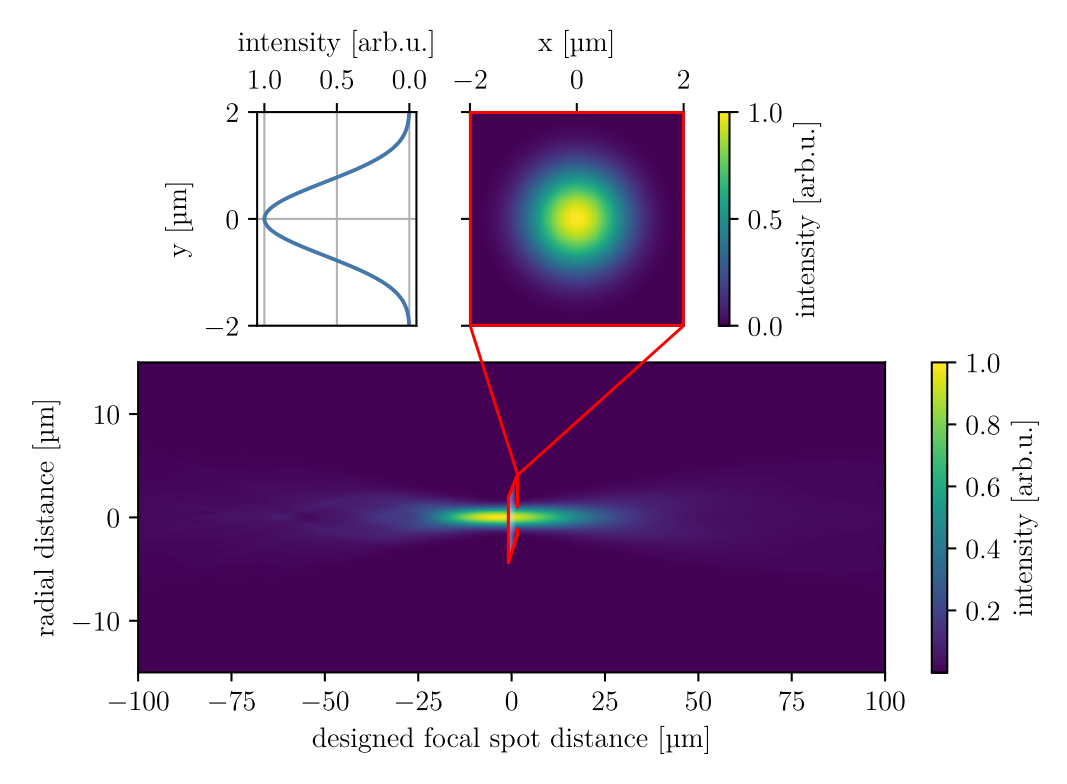


Figure 4.4: Simulated linear intensity profile of an AlN metalens with a numerical aperture of 0.1.

In accordance with Eq. 2.7, we compared the power of the beam reaching close proximity to the determined focal spot to the incident power to estimate the efficiency of this design. This approach revealed a value of 65%. A substantial part of the reduction of the initial power stems from absorption in and reflection at the dielectric, as apparent from the transmission curve in Fig. 4.3. The residual reduction is illustrated by converting to a logarithmic scale, as depicted in Fig. 4.5. It is discernable that a portion of the incident light does not reach the focal spot, but is distributed around it or scattered in a different direction.

In addition to these losses, a slight deviation from the designed focal length is notable, which is most distinct in Fig. 4.4. The minimal beam waist gravitates towards the lens plane. This phenomenon is likely associated with the number of Fresnel zones present within the lens and will be discussed further in Sect. 4.3.3.

As outlined in Sect. 2.3, the previously derived efficiency represents the fraction of redirected incident light across all involved deflection angles plus non-diffracted radiation. The latter denotes light that traverses the lens unaltered. To attain a more precise measure of the redirection efficiency, it is necessary to evaluate only the highest involved angles while excluding non-diffracted light. Accordingly, we engineered a blazed grating to deflect the beam away from the non-diffracted fraction at an angle of $\theta = 5.7^{\circ}$. This value corresponds to the maximum opening half-angle of the present 0.1 numerical aper-

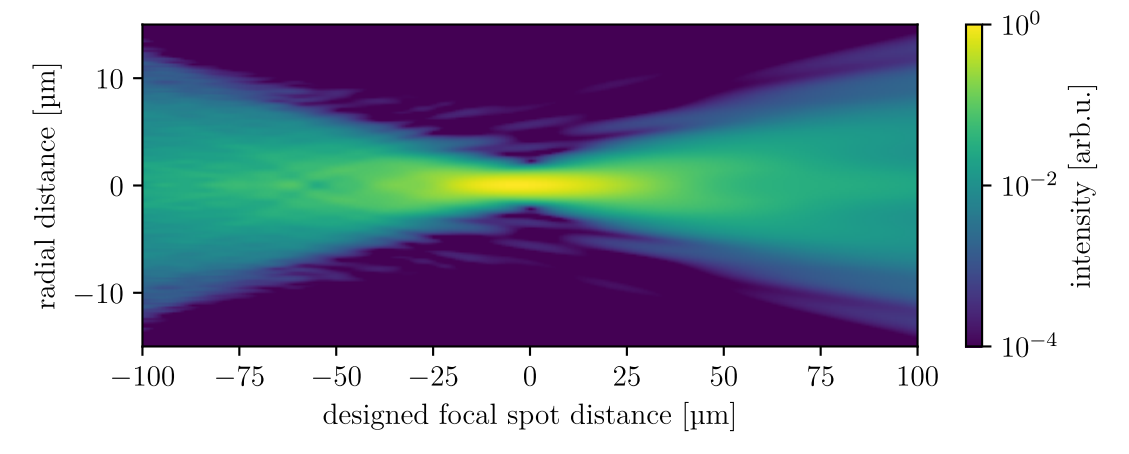


Figure 4.5: Simulated logarithmic intensity profile of an AlN metalens with a numerical aperture of 0.1.

ture metalens (Eq. 4.2). Substituting θ into Eq. 2.6 generates the requisite phase profile, which, akin to the previous design, can be translated into meta-atoms and incorporated into the FDTD simulation cell. Unlike the preceding simulation, larger metasurfaces offer no additional informational value. Consequently, we reduced the cross-sectional cell size to $10x10\,\mu m$.

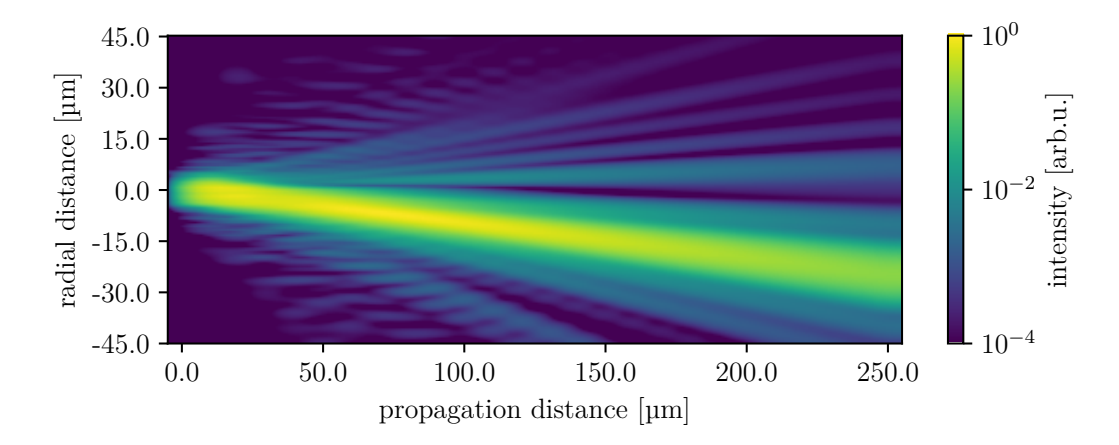


Figure 4.6: Simulated logarithmic intensity profile of an AlN blazed grating with a deflection angle of $\theta = 5.7^{\circ}$.

Figure 4.6 visualizes the resulting logarithmic intensity profile from the specified grating parameters. To ensure the separation of the redirected beam from the non-diffracted fraction, we selected a camera distance of $250\,\mu\text{m}$, resulting in a separation of the redirected light by $25\,\mu\text{m}$, from the incident beam, which is readily observable in the plot. Intensity analysis in the camera plane yielded a redirection efficiency of 61%, falling slightly short of the 0.1 NA metalens. Nevertheless, the proximity of these values sug-

gests the predominant redirection of incident light, with only a minor portion unaffectedly passing through the lens. Additionally, possible aperture effects induced by the reduction of the simulation cell size may also be a contributing factor, which will be elaborated in Sect. 4.3.3.

4.3.2 High-Aperture Lens

We designed the second AlN UV metalens with a NA of 0.5. Following the same procedure as in the prior section, a focal length of 20 μ m with a diffraction-limited focal spot size of $w_{d.l.} = 0.45 \,\mu$ m was determined. Integration of the design into the FDTD simulation, followed by far-field transformations, provided the logarithmic intensity profile depicted in Fig. 4.7. The analysis of the profile reveals a focal beam waist of $w = 0.61 \,\mu$ m, which captured 54% of the incident intensity in its vicinity.

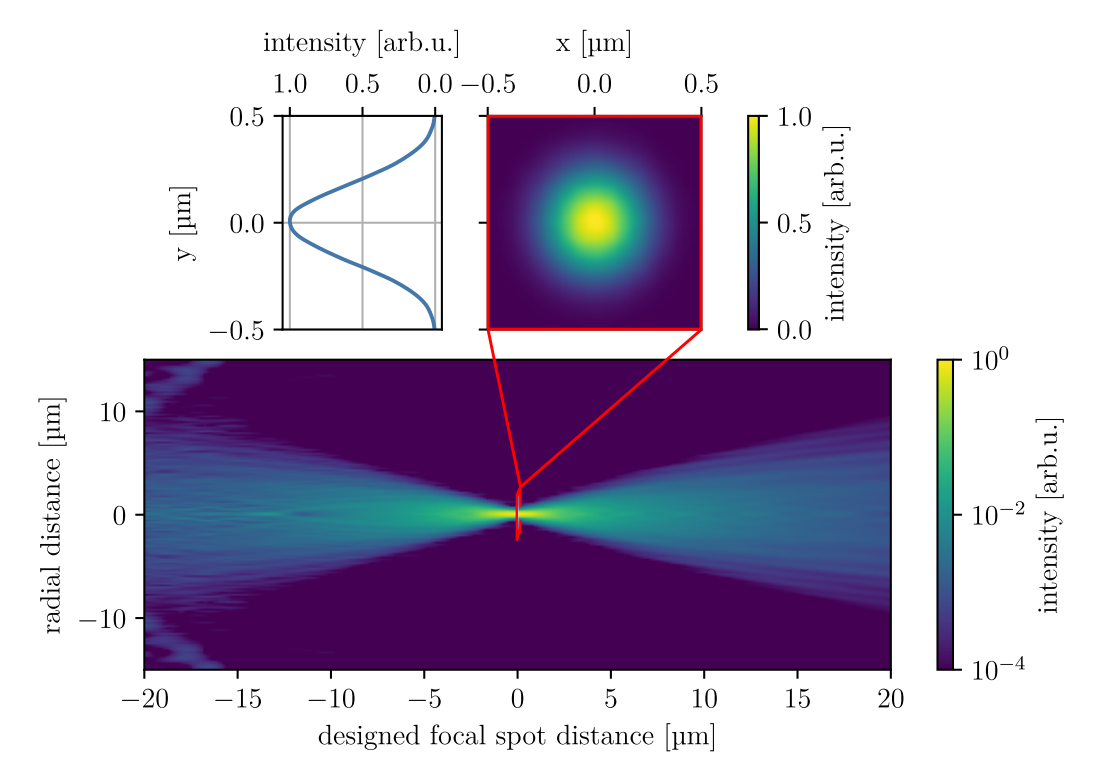


Figure 4.7: Simulated logarithmic intensity profile of an AlN metalens with a numerical aperture of 0.5.

Upon initial examination of Fig. 4.7, the majority of the intensity appears concentrated around the focal spot. However, slightly concealed at the periphery near the lens plane, diffraction losses divert a fraction of the incident light away from the optical axis. This effect most probably stems from an unintended periodicity of the metalens, which could be induced by the rapid fluctuation of the phase profile between adjacent Fresnel zones. Following an equivalent approach as in the preceding section, we simulated a blazed

grating featuring a maximum opening half-angle of $\theta=26.6^{\circ}$ to assess the impact of higher angle redirection on the overall efficiency. The resulting intensity profile is depicted in Fig. 4.8. As illustrated in the plot, to repeatedly achieve a separation of 25 µm from the non-diffracted fraction, we selected a camera distance of 50 µm. An analysis of the intensity profile at the camera plane revealed a redirection efficiency of 42%, representing a 19% reduction compared to the previous angle of 5.7°. One reason for the decrease in efficiency is the less accurate phase sampling for increasing angles, as detailed in Sect. 2.3, and was expected. This reduction in efficiency for increasing angles also affects the high-aperture metalens. Accordingly, in addition to the already discussed diffraction losses, high-angle losses further contribute to the reduced efficiency observed in the high-aperture design compared to the low-aperture one.

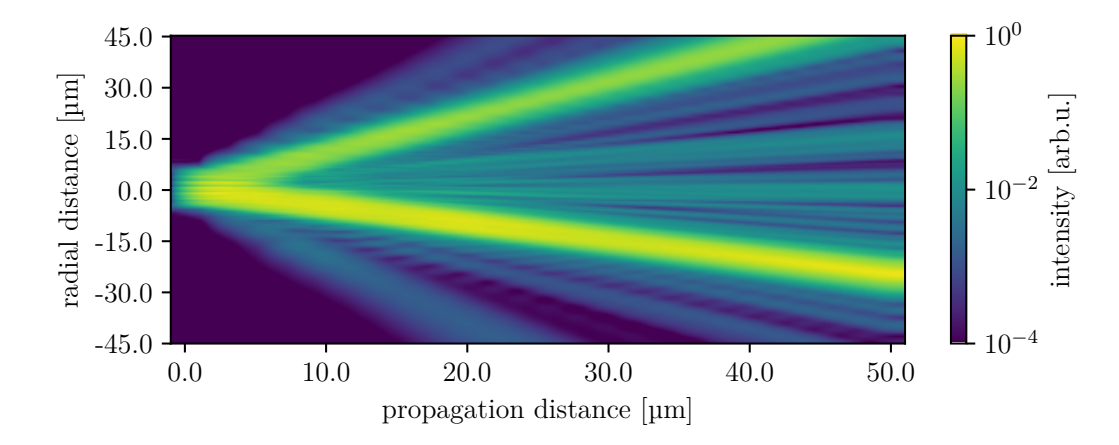


Figure 4.8: Simulated logarithmic intensity profile of an AlN blazed grating with a deflection angle of $\theta = 26.6^{\circ}$.

The second, and more visually prominent, reason for the decreased redirection efficiency in Fig. 4.8, is the unforeseen but substantial second transmission direction, which meets the camera plane at $y \approx 55\,\mathrm{\mu m}$. Its origin can be derived by considering k-space and the conservation of momentum [37]: A spatial periodicity Δ has the potential to change the momentum of transmitted light by $k = \frac{2\pi}{\Delta}$, however, diffraction modes can only be excited by a grating if $|\mathbf{k}_{\text{initial}}| = |\mathbf{k}_{\text{final}}|$ is fulfilled. Given the present unit cell where $\Delta_{\text{uc}} < \lambda$, only $m\mathbf{k}_{\text{uc}}$ with m=0 satisfies momentum conservation. However, through the introduction of the blazed grating, an additional periodicity $\Delta_{\text{blaze}} = 1.15\,\mathrm{\mu m}$, and thus momentum k_{blaze} , is introduced. Again applying the conservation of momentum and accounting for the remaining longitudinal momentum k_{after} , we obtained Eq. 4.6, which can be satisfied for m=1 and n=-1. Implemented in Fig. 4.8, thus a parallel beam propagating along the x-axis, diffracted in +y, this yields $\theta = \arcsin\left(k_y^{\text{final}}/k_x^{\text{final}}\right) \approx 47^{\circ}$, which closely matches the second observed diffraction angle.

$$|\mathbf{k}_{\text{initial}}| = |\mathbf{k}_{\text{final}}| = \sqrt{m\mathbf{k}_{\text{uc}}^2 + n\mathbf{k}_{\text{blaze}}^2 + \mathbf{k}_{\text{after}}^2}$$
 (4.6)

4.3.3 Discussion

As previously stated, the determined focal length of the high-aperture metalens (B) aligns with the designed length, while it is shifted towards the lens plane for the low-aperture metalens (A). This correlation between the numerical aperture and the observed aberration may be attributed to the number of involved Fresnel zones.

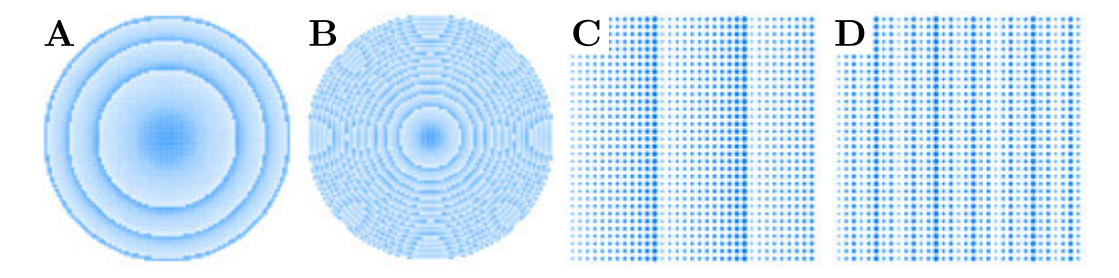


Figure 4.9: 2D layouts of all simulated metasurfaces. A) and C) lens and blazed grating with NA = 0.1, B) and D) lens and blazed grating with NA = 0.5.

As illustrated in Fig. 4.9, this number differs significantly between the low- and high-aperture lens layouts. Each added Fresnel zone introduces wavefronts spanning the total phase spectrum of 2π into the superposition that forms the beam profile. This could have a twofold effect: it adds information, but also increasingly randomizes phase profile sampling [37]. Accordingly, due to the steep phase gradient within each Fresnel zone, the transmission minima observed in the phase map (Fig. 4.3) and potentially other sources of aberrations may average out. Alternatively, the focal shift might be concealed by the decreased focal length. Either way, due to the limitations of the computational cell size, both theories are challenging to prove.

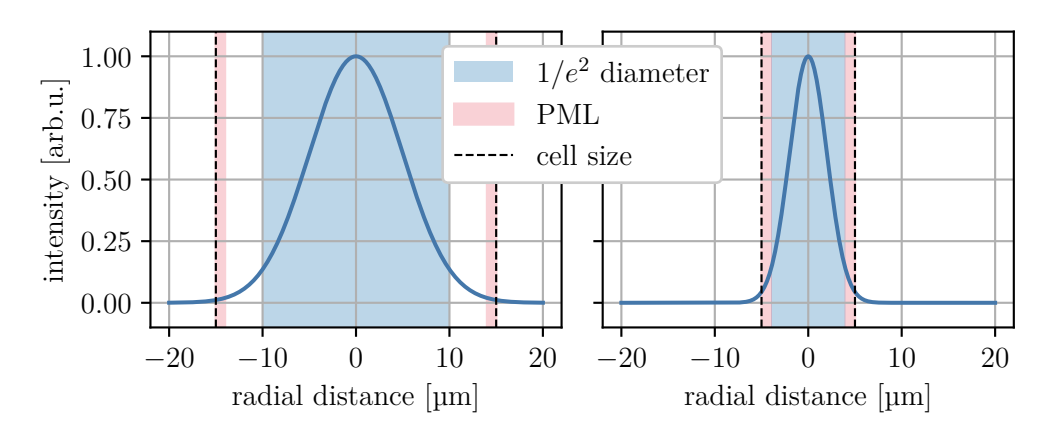


Figure 4.10: Cross-section of the initial Gaussian intensity distribution within the simulation cell of the metalenses (left) and the blazed gratings (right).

Apart from the aforementioned aberration, phase sampling may also be a contributing factor to the observed reduction in efficiency for large redirection angles. A comparison of the low- (C) and high-angle (D) blazed grating effectively illustrates the substantially decreased sampling per Fresnel zone for the higher angle layout.

A hitherto unmentioned peculiarity of the simulation pertains to the Gaussian intensity distribution of the incident beam. Given the finite size of the FDTD simulation cell, losing a fraction of the peripheral intensity is unavoidable. This phenomenon resembles the truncation that would be induced by an aperture placed in front of the metalens. Figure 4.10 illustrates this situation via a cross-section of the initial Gaussian intensity distribution within the simulation cell. For the metalenses (left) and the blazed gratings (right) integration revealed that 1% and 5% of the incident power are lost.

As the focal plane of a lens corresponds to the Fourier transform of the aperture opening function, the truncation induces a reciprocal effect on the generated focal spot. This enlarges the focal beam waist, which aligns with the observed deviation from the diffraction-limited focal spot size. The more pronounced truncation of the blazed gratings mainly manifests in diffraction effects observed in the vicinity of the central lobe.

5 Fabrication

The results from the previous chapter regarding the efficiency of both the 0.1 and 0.5 NA metalens designs indicate their potential for a practical realization. As alluded in Sect. 3.2 an unexplored, however promising approach to metalens engineering is the atomic layer deposition (ALD) of AlN meta-atoms. This fabrication route, illustrated schematically in Fig. 5.1, necessitates the preparation of a template that serves as a foundation for ALD (steps 1 and 2). We achieved the resolution for template feature sizes from 75 to 225 µm by electron beam lithography (EBL), which will be discussed in Sect. 5.1. With unit cells of 300 nm collectively forming a targeted 100 µm diameter lens, the desired optics encompass more than 10⁶ elements. A visualization of the design across different magnifications is depicted in Fig. 5.2 [38].

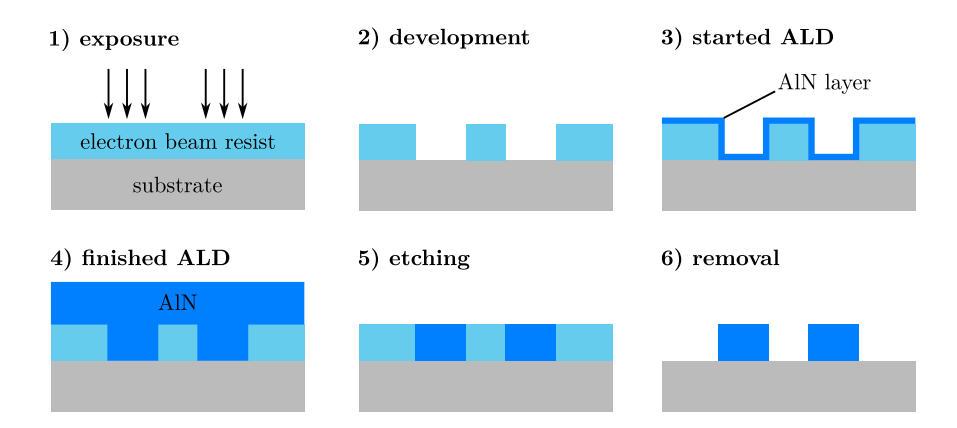


Figure 5.1: Schematic representation of the fabrication steps involved in the realization of AlN metalens designs [38].

We pattern the positive electron beam resist AR-P 6200.13 (CSAR 62) from Allresist GmbH with the EBL system eLINE Plus by Raith GmbH. This system was provided by the Institute of Physics at the University of Graz, with essential operational and functional insights contributed by Andreas Hohenau and Joachim Krenn. The resist was newly acquired, and no established protocols were available, therefore we developed a new workflow from the ground up. The needed fundamental concepts, preparatory work, the employed fabrication methodology, as well as the results leading to the realization of the aforementioned template will be outlined in the following sections. For the subsequent fabrication steps illustrated in Fig. 5.1, involving the actual ALD process (3 and 4), as well as the reactive ion etching (5) to the desired structure height, we are currently waiting for collaborators.

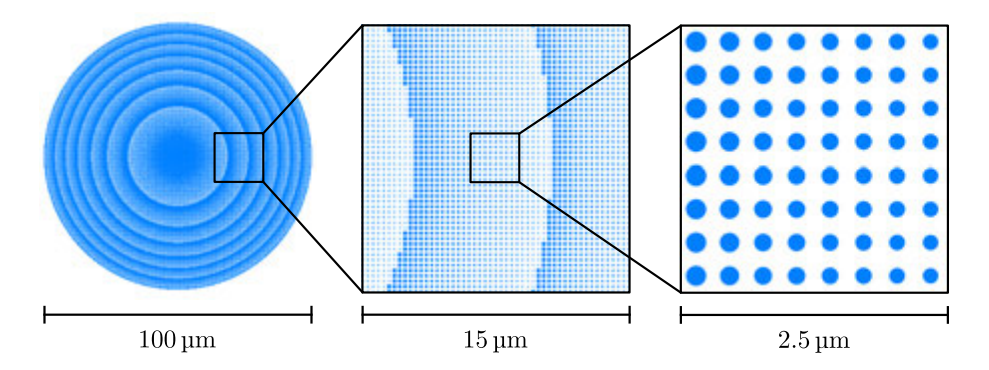


Figure 5.2: Visualization of a 100 μm diameter metalens layout across different magnifications.

5.1 Electron Beam Lithography

As shown in Eq. 5.1, the (non-relativistic) de Broglie wavelength of an electron depends on its velocity (thus the acceleration voltage U acting on the charged particle) [39, p. 26].

$$\lambda_{e^{-}} = \frac{h}{\sqrt{2meU}} = \frac{1.226}{\sqrt{U}} \text{ [nm]}$$
 (5.1)

Electron Beam Lithography (EBL) exploits the matter wave of an electron to locally illuminate a sample, thereby altering the chemical structure of a so-called resist. This chemical transformation weakens or strengthens the illuminated part of the resist, which, through development, yields the desired structure. Instead of a mask-based parallel illumination system (as used in optical lithography), a beam of electrons is scanned over the sample, rendering EBL a direct write approach. This comes with the advantage that the complicated production of a mask is obsolete, yet is tempered by the drawback of lower throughput. As in scientific research, the latter is hardly of importance, EBL is an excellent tool for the scope of this thesis.

In optical lithography, as well as in EBL, the deposited energy from the (matter-)wave causes bond interactions that lead to the aforementioned alterations of the resist layer. Though the involved radiation chemistry is complicated and material dependent, the macroscopic effects can be summarized in four main characteristics [39, pp. 47-51]:

- Tone: Generally split into two groups: For positive tone resists, illumination causes a structural weakening, whilst in negative tone resists a structural strengthening is achieved. Thus, the two types of tones generate inverse results.
- Sensitivity: A measure for the minimum dose (EBL: charge/area) to achieve structural alterations.
- **Resolution:** The minimal dimensions of features that are realizable with the resist in use. In contrast to the previously mentioned diffraction limits, the main limitation in this context is the resist itself (grain size, roughness, etc.).

• Contrast: Defines how distinct the differentiation between exposed and unexposed areas is, consequently impacting the achievable resolution.

It is important to note that the success of pattern transfer is influenced not only by the aforementioned characteristic parameters, but also factors such as adhesion and proximity effects (Sect. 5.3.2). Additionally, the compatibility with subsequent processing steps, including properties like etch resistance, must be taken into account.

5.2 Preparatory Work

Prior to patterning the simulated design, two preparatory steps must be established: the controlled deposition of a resist film on the substrate and the conversion of the design into a format compatible with the EBL system. For the former, precise control over the film thickness is crucial for the subsequent fabrication steps. To achieve this, we utilized spin coating. Given that no preliminary work in our lab had been done with the resist at disposal, the first step was the investigation of the spin curve, which describes the deposited film thickness in dependence of the rotational speed involved in the spin coating process. Regarding the conversion, the binary database file format GDSII was selected. The following sections detail the involved methodology and results of this preparatory work.

5.2.1 Electron Beam Resist Spin Coating

The general process of spin coating involves the application of a resist in a solvent to a substrate, which is subsequently spun at a specific rotational speed. The centrifugal force generated by this spinning action causes the solution to spread outward and be flung off the substrate, thereby thinning the viscous layer. This thinning is counteracted by adhesion. The equilibrium between these forces determines the film thickness, which can thus be precisely regulated by adjusting the rotational speed of the substrate. The evaporation of the residual solvent leaves behind a solid film of electron beam resist, which is then ready for further nanofabrication. Following this principle, resist films were deposited at various rotational speeds. We determined and subsequently fitted their corresponding thicknesses with the profilometer KLA-Tencor D-500, which was provided by Peter Hadley of the Solid State Physics Institute at Graz University of Technology. The resulting continuous spin curve is depicted in Fig. 5.3 and henceforth functions as the starting point for all following process steps. As previously demonstrated (Fig. 4.2), a meta-atom height of 400 nm offers the most favorable compromise between phase shift and transmission. Transcribing this height based on the spin curve reveals a spin speed of 4500 rpm for the required film thickness.

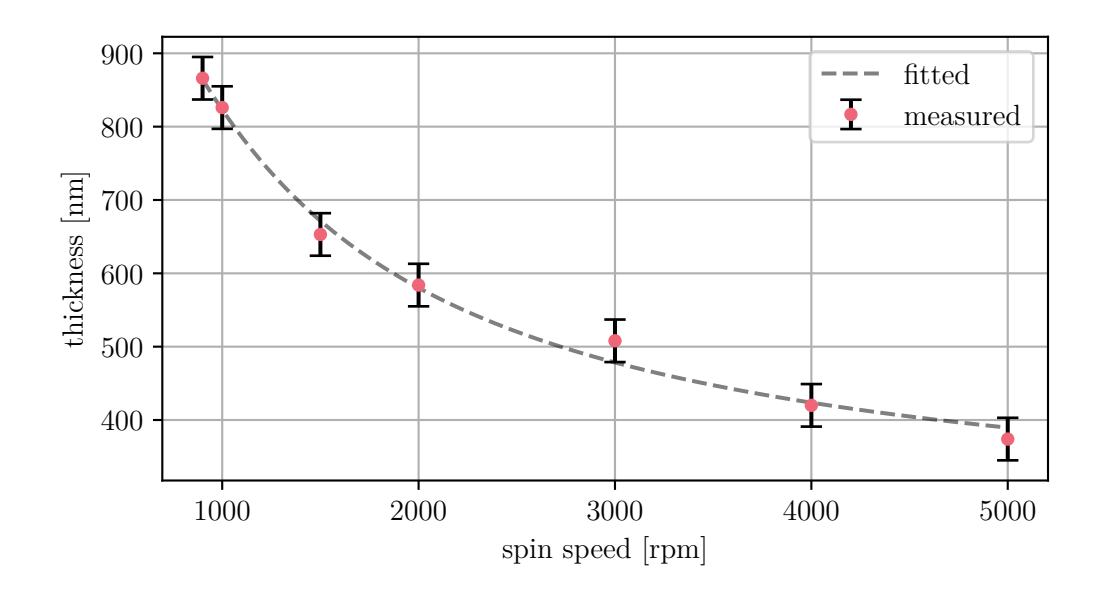


Figure 5.3: Measured and fitted spin curve of the electron beam resist AR-P 6200.13 (CSAR 62). The error bars represent the standard deviation for each measurement.

5.2.2 Data Preparation

We converted the simulated design into the EBL-compatible GDSII format using the Python package GDSII Tool Kit (gdstk). It allowed for the seamless integration of all design features into the binary database file, which due to its well-established status in the nanofabrication industry, ensures compatibility across systems and straightforward visualization. However, the GDSII format caused instabilities in the EBL system software. We circumvented these instabilities by converting further to Raith's ASCII file format, which is exemplified in Tab. 5.1.

Table 5.1: Excerpt on the system-specific ASCII file format from the software manual of the EBL system eLine Plus from Raith.

GDSII element	Syntax	Comment
polygon	1 (dose) (layer) $(x_1) (y_1)$ $(x_2) (y_2)$	coordinates of 1st vertex coordinates of 2nd vertex
	$ \begin{array}{c} \dots\\ (x_1) \ (y_1)\\ \# \end{array} $	repeated 1st vertex end of element

5.3 Fabrication Methodology

Building upon the computational insights and the preliminary work discussed previously, the present chapter delves into the fabrication steps employed for the realization of the ALD template. Therein, we selected 1-inch UV-grade fused-silica wafers (JGS1) with a thickness of $(500 \pm 25) \, \mu m$, supplied by MicroChemicals GmbH, as the substrate (Sect. 3.2). These wafers served as foundation for all subsequent processing steps, which are visually represented by the workflow diagram in Fig. 5.4. Several comments concerning the elements in the diagram are noted below.

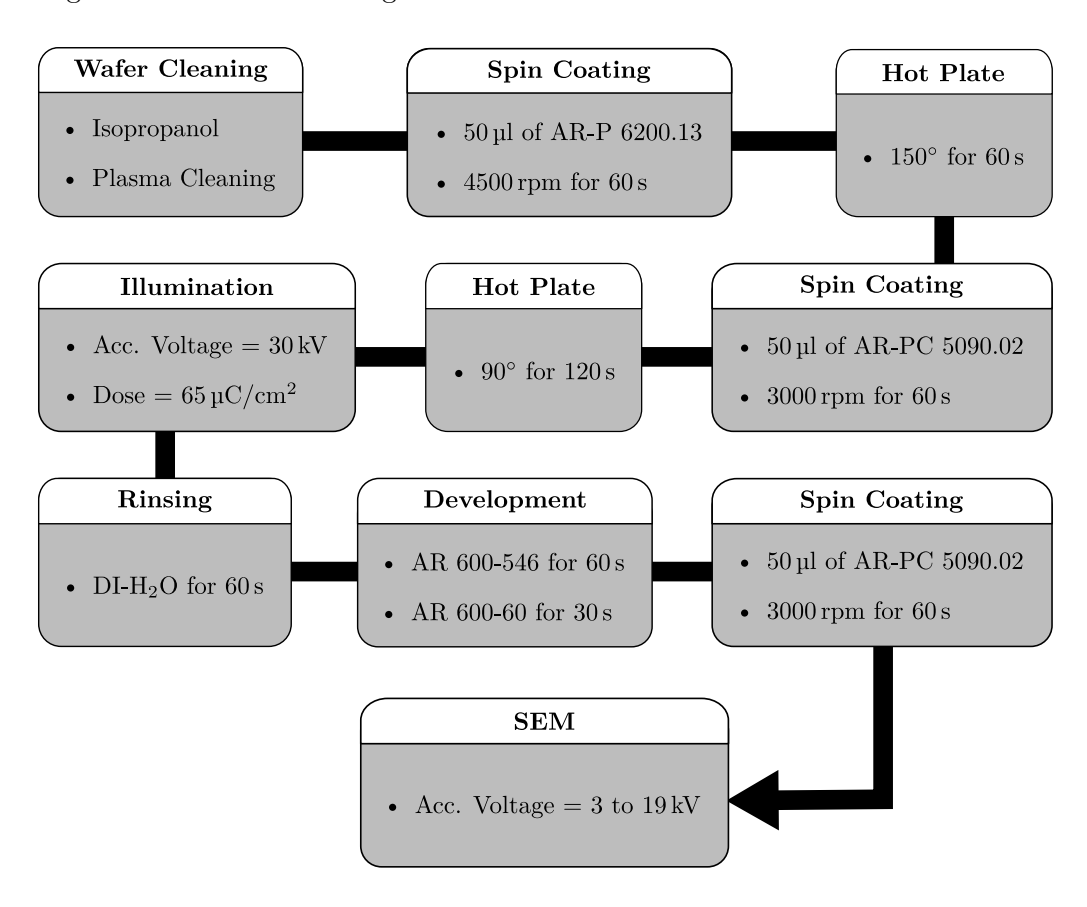


Figure 5.4: Workflow diagram of the ALD template fabrication process.

- The resist at disposal, designated AR-P 6200.13 (CSAR 62) by Allresist GmbH, is a positive electron beam resist. Consequently, electron exposure compromises its structural integrity, enabling the subsequent removal of illuminated fractions.
- With feature sizes below 1 µm, scrupulous cleaning of the SiO₂ wafers is essential. Inter alia, we utilized ambient air and O₂ plasma cleaning to remove contaminants and enhance the adhesion of the resist to the substrate.

- Neither the resist nor the substrate are conductive. In order to prevent charging during electron exposure, we spin coated an additional conductive layer of AR-PC 5090.02 (Electra 92). This layer dissipates charges without affecting the patterning process, and it can be easily removed before development by rinsing the substrate with deionized water.
- The EBL system is simultaneously employed as scanning electron microscope (SEM). Accordingly, we generated all captured images by exposure to an electron beam. As the weakening of the resist does not differentiate between patterning and imaging, the SEM process damages the ALD templates. Hence, only samples that are not designated for further processing can be observed.

5.3.1 Dose Test

With regard to the actual patterning process, the stated dose of $65\,\mu\mathrm{C/cm^2}$ (suggested by Allresist GmbH) can only be regarded as a reference point. The ideal exposure dose can significantly deviate from this reference, depending on the structure of interest. Similarly to the previously discussed spin curve, no prior knowledge of the ideal exposure dose for the resist was available, thus we conducted test across various doses.

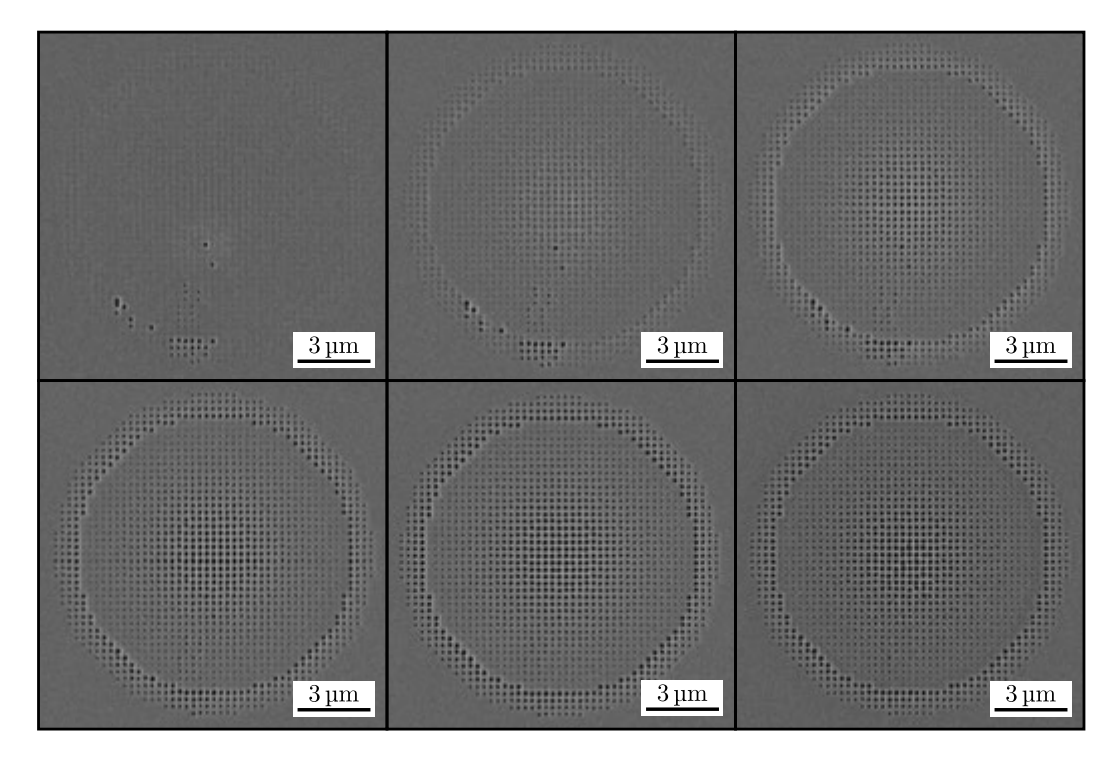


Figure 5.5: Test series on electron beam resist CSAR 62 across multiple exposure doses ranging from from 45 to $105\,\mu\text{C/cm}^2$ with an increment of $12\,\mu\text{C/cm}^2$.

Figure 5.5 presents such a series, with doses ranging from 45 to $105 \,\mu\text{C/cm}^2$ with an increment of $12 \,\mu\text{C/cm}^2$. As anticipated, the lowest doses were unable to fully solubilize

the resist, while the highest doses created breaches between the widest features. It is noteworthy that the templates exhibited a dose bias by the EBL system towards the lower left quadrant. This effect is most evident in the template that received the least exposure (upper right corner). Although the majority of its structures were underexposed, specific sites were overexposed as a result of this unintended bias.

Unimpeded by this imperfection, a dose of approximately $90\,\mu\text{C/cm}^2$ (Fig. 5.5, bottom center) best reproduced the design. However, this does not apply to the smallest perforations, which receive substantially lower doses due to the size-proportionality of proximity effects.

5.3.2 Proximity Correction

Beam broadening caused by scattering and secondary electrons leads to inadvertent exposure of the area surrounding written structures, compromising the fidelity of an intended pattern and counteracting the resolution suggested by the de Broglie wavelength (Eq. 5.1). The various interactions, that cause this broadening are summarized under the term proximity effect and schematically depicted in Fig. 5.6.

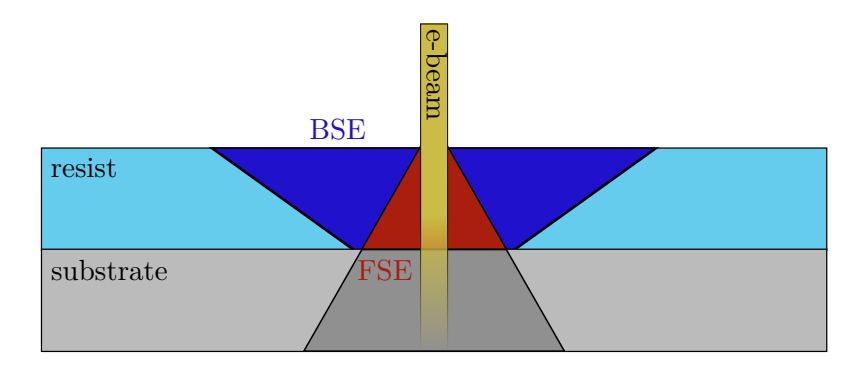


Figure 5.6: Schematic representation of the cross-sectional area that is influenced by proximity effects from forward (FSE) and backscattered electrons (BSE).

It contains the complex interplay of forward scattering within the resist, backscattering from resist and substrate, interaction mechanisms between the electrons and molecules, as well as, post-exposure development specifications. Each of the aforementioned effects possesses intricacies that collectively impede precise predictions. The suggested point spread function f(r) in Eq. 5.2 should therefore only serve as an approximation for the most fundamental scenario. Therein, it is described by the weighted sum of two Gaussians for each, forward- and backscattered electrons. Depending on the involved materials and dimensions, the function is expanded with terms that more accurately model energy-dependent development arising from the deceleration of electrons.

With the point spread function, it is possible to modulate the original design based on pattern adjacency, thus counteracting the proximity effect and depositing uniform doses [39, pp. 95-98].

$$f(r) = \frac{1}{\pi(1+\eta)} \left(\frac{1}{\alpha^2} \exp\left[-\left(\frac{r}{\alpha}\right)^2 \right] + \frac{\eta}{\beta^2} \exp\left[-\left(\frac{r}{\beta}\right)^2 \right] \right)$$
 (5.2)

where:

r = lateral distance from incident beam

 α/β = standard deviation of forward/backscattered electron distribution

 η = ratio of deposited energy between forward and backscattered electrons

The parameters governing Eq. 5.2 are derived from Monte Carlo simulations. They are modeled based on statistical interactions that consider factors such as acceleration voltage and resist/substrate composition to approximate cross-sections and, hence, are system-specific [39, p. 97]. Figure 5.7 illustrates an exemplary Monte Carlo simulation, yielding the statistically deposited energy inside the resist.

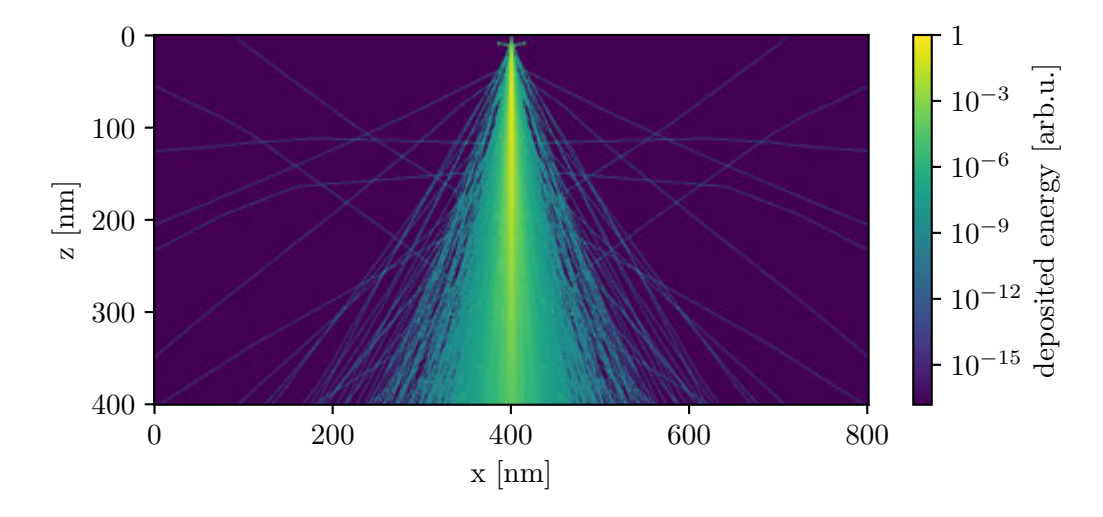


Figure 5.7: Exemplary energy deposition of an electron beam inside the resist.

The electron beam lithography machine illuminates the sample using a discrete grid based on a certain step size and dwell time. While the former represents the theoretical resolution (neglecting the true beam diameter), the latter controls the deposited charge per grid point. The discrete nature of this process results in a reduction of grid points for decreasing feature sizes. Consequently, fewer grid points fall within areas affected by local proximity effects, thereby decreasing the locally deposited dose.

Figure 5.8 (left) illustrates the practical impact of this behavior. The majority of features within the image are fully developed, whereas those with the smallest diameter remain underexposed. Accordingly a correction of the proximity effect aims to decrease doses of wide, closely packed or central structures, while increasing the dose of small, spread-out or peripheral structures. The resulting template after such a correction is depicted in Fig. 5.8 (right) and demonstrates an equal development across all feature sizes. Notably, the slight warping of broader structures is not intrinsic to the fabricated

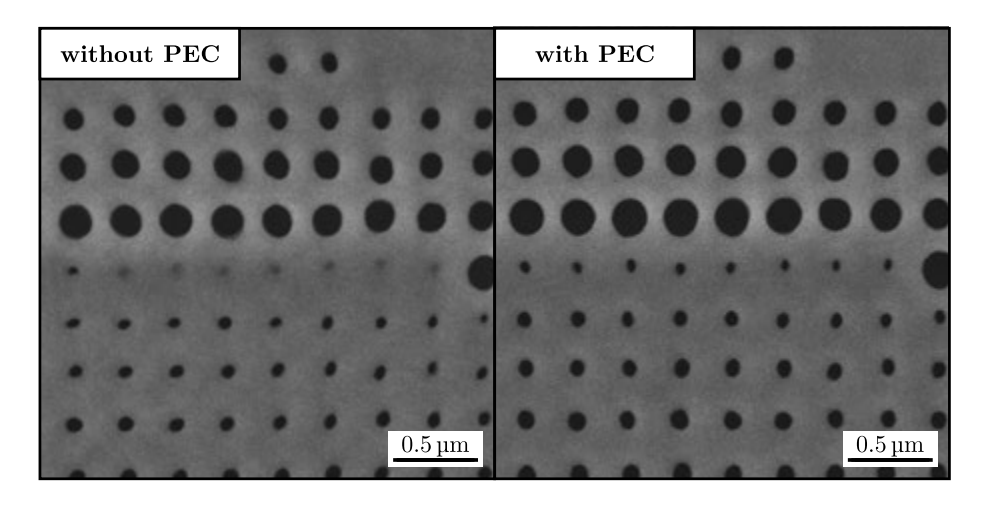


Figure 5.8: Comparison of an ALD template with and without proximity effect correction.

template but introduced during imaging, highlighting the necessity of swift image capture. The utilized proximity effect correction parameters stem from the EBL system software NanoPECSTM. Based on the point spread function in Eq. 5.2, and the determined statistical energy distribution, the resulting values were $\alpha = 2 \, \mathrm{nm}$, $\beta = 1590 \, \mathrm{nm}$, and $\eta = 0.72$.

5.4 Fabrication Results

Following the presented methods, we fabricated four ALD templates, corresponding to the simulated low-aperture (NA = 0.1) and high-aperture lens (NA = 0.5), along with their respective blazed gratings. Figure 5.9 illustrates images of these templates.

As outlined earlier, we selected a lens diameter and lateral grating length of 100 µm. According to Eq. 4.2, this selection mandates focal lengths of 500 µm for the low-aperture lens and 100 µm for the high-aperture lens. The initial inspection indicates successful patterning of all four designs, with a high degree of resemblance to the targeted layout. Figure 5.10 provides a more detailed view, confirming this observation of the templates. Measurements of the cylindrical elements' true diameter revealed a minor enlargement from the targeted layout. Concerning the smallest (75 nm) and largest features (225 nm), we observed deviations of approximately 5 nm and 15 nm, respectively. This increase for larger elements most probably results from the imaging process affecting the integrity and stability of the resist. Larger perforations are surrounded by less supporting material, thus disintegrate faster. Therefore, the true diameter, particularly of the larger perforations, is likely to be closer to the target than it appears during the imaging process.

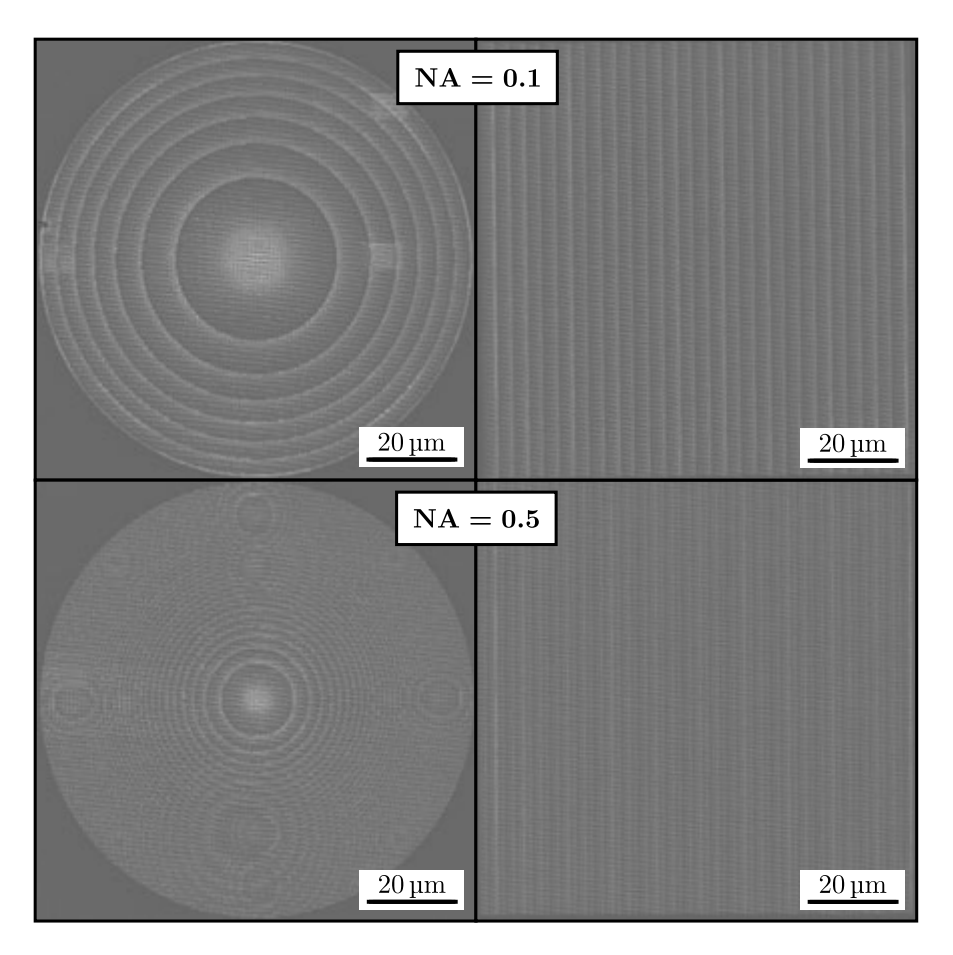


Figure 5.9: SEM images of fabricated metalens ALD templates (left) and blazed grating templates (right).

Apart from these minimal, potentially imaging-induced deviations, the overall correspondence between the generated pattern and the desired GDSII layout (Fig. 5.11), meets all requirements. As stated at the beginning of this chapter, further progress in the realization of an AlN metalens is, however, contingent upon a collaborator that provides the ALD system required for the subsequent fabrication steps.

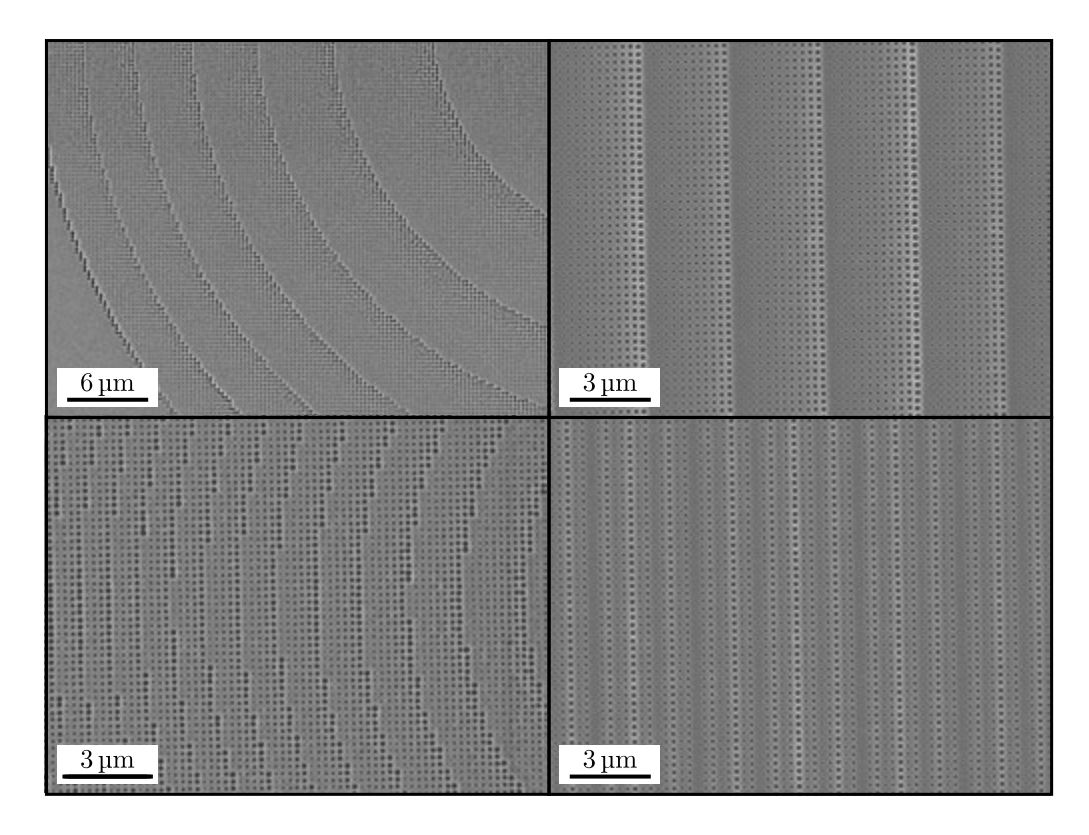


Figure 5.10: Detailed SEM images of fabricated templates, corresponding to Fig. 5.9.

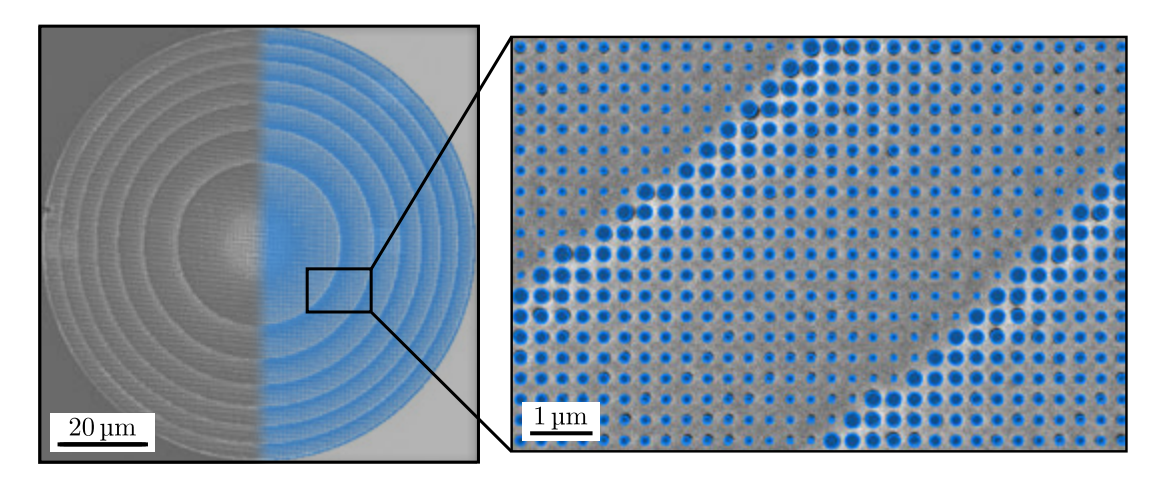


Figure 5.11: Superposition of the targeted GDSII layout and the fabricated ALD template (0.1 NA metalens design).

6 Proof of Concept - Resist Metalens

This chapter presents a proof of concept, demonstrating the feasibility of fabricating functional metalenses using the previously established principles and methods. In particular, we substituted the electron beam resist CSAR 62 as the dielectric and thus directly employed it as the metastructure. Motivated by its transparency and refractive properties, the objective was the fabrication of a resist-based metalens for the visible spectrum by adaptation of the prior strategies. The validation of its function will serve as a proof of concept, supporting the precision, performance, and hence the broader aims of this thesis. Akin to the methodology of the preceding chapters, we employed the following key steps:

- 1. **Design and Simulation:** FDTD simulations were utilized to optimize meta-atom dimensions and generate phase maps. This data was subsequently used to design a metalens based on Eq. 2.4.
- 2. **Fabrication:** The simulated design was patterned into the resist using electron beam lithography. In order to ensure comparability, all previous processing steps were revisited, including the use of SiO_2 as a substrate due to its optimal optical properties for both the UV and visible spectrum.
- 3. Characterization: As the patterned structure already resembles a functional metalens, its optical properties can be directly assessed. Accordingly, beam profile and focal plane measurements similar to those observed in the preceding simulations were conducted experimentally. In order to achieve this we constructed a custom experimental setup.

6.1 Design and Simulation

The fabrication of the resist-only metalens design is a one-step process, as the desired pattern can be directly inscribed into the resist using electron beam lithography. The available resist, CSAR 62, is a positive resist, of which, exposed areas are removed during development. While this was advantageous for the AlN templates, utilizing the resist as the active dielectric necessitates an inversion of the template layout in order to obtain a comparable structure after the fabrication without the subsequent ALD. However, instead of directly inverting the layout, we adjusted the unit cell's position within the periodic grid, thereby preserving the cylindrical symmetry of the exposed structures. In essence, the non-exposed cross-shaped volume encircled by four adjacent exposed cylinders transforms into the new meta-atom, as schematically illustrated in Fig. 6.1.

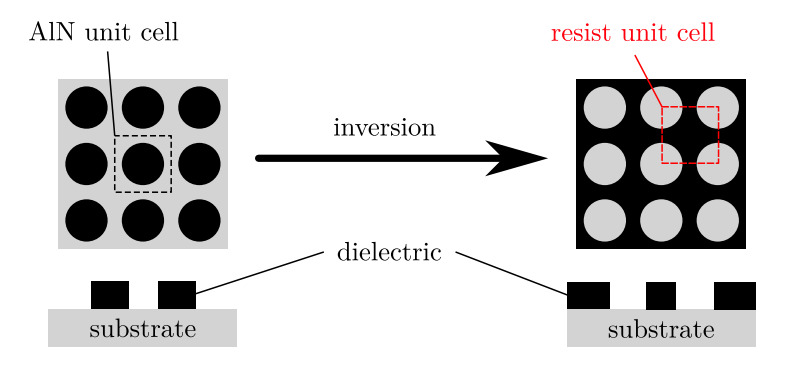


Figure 6.1: Conceptional inversion from AlN template to resist-only metalens design in top view (top) and as cross-sectional slice (bottom).

Concerning the resist's refractive properties, the dispersion of its refractive index $n(\lambda)$ can be described by the empirical Cauchy equation (Eq. 6.1). The coefficients were provided by Allresist GmbH and amount to $n_0 = 1.543$ and $n_1 = 7140$ [40].

$$n(\lambda) = n_0 + \frac{n_1}{\lambda^2}$$
 where $[\lambda] = \text{nm}$ (6.1)

At a targeted wavelength of 633 nm, this yields a refractive index of 1.561, just exceeding the self-imposed limit for potential UV dielectrics of n > 1.5 (Tab. 3.1). The achievable range of effective refractive indices (Sect. 4.1) is further constrained by incorporating a minimal feature size of $x_{\min} = 75 \text{ nm}$.

A similar argument as for the AlN templates resulted in an in-plane unit cell dimension of $a=500\,\mathrm{nm}$. Given these design limitations, the theoretical hole diameters range from 75 to $630\,\mathrm{nm}~(=\sqrt{2}a-x_\mathrm{min})$. As the diameter approaches the upper limit, the overlapping cylinders encircle a shrinking four-cusped hypocycloid. However, fabrication trials revealed substantial fragility of these free-standing elements. To ensure a robust design, we adjusted the upper diameter limit to $450\,\mathrm{nm}$, connecting the cross-shaped meta-atoms with at least $50\,\mathrm{nm}$ bridges at the cusps, as illustrated in Fig. 6.2. While this adjustment improved design integrity, it further decreased the effective index range to [1.243, 1.557] (Eq. 4.1).

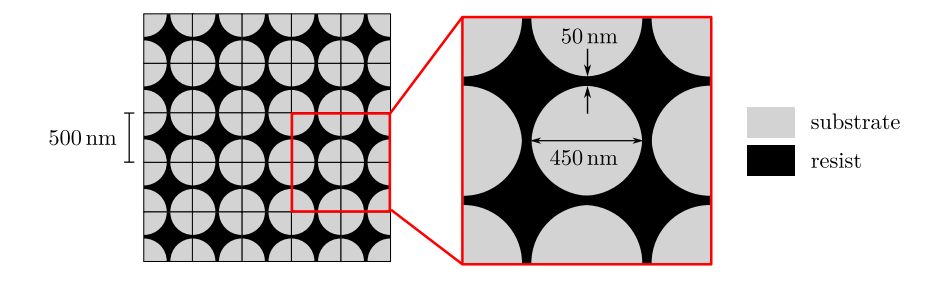


Figure 6.2: Top view and hole diameter limit for resist-only metalens design.

Despite the limited range, we conducted FDTD simulations across various meta-atom form factors, in accordance with the methodology in Sect. 4.1, to accumulate the corresponding phase maps. It should be noted that Allresist GmbH did not provide data on the resist's extinction coefficient. However, given its visible transparency, we assume that the extinction coefficient is negligible. Figure 6.3 presents the resulting data for different film thicknesses: Taller elements induce larger relative phase shifts due to increased path lengths, while transmission remains acceptable across all dimensions. These results indicate that taller structures can compensate for the limited range of effective refractive indices. However, the viscosity of the resist restricts the maximum film thickness per spin coating cycle to approximately 850 nm (Fig. 5.3). While multilayer coating is a potential solution, it presents new challenges related to conformality and adhesion. Therefore, we used a single 850 nm thick layer. Considering all relevant parameters listed below, the maximum induced phase shift falls marginally short of π .

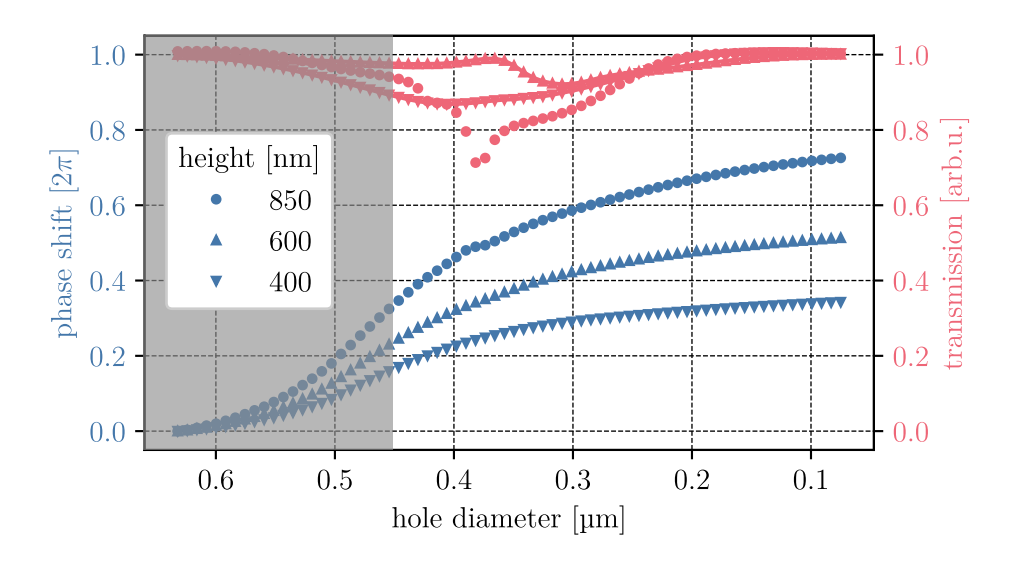


Figure 6.3: Resulting phase map and transmission of resist-only meta-atoms at various heights and a unit cell size of 500 nm. Restricted diameters due to fabrication compromises are greyed out.

Given that only approximately half of the full 2π phase coverage is available to the metalens, its phase profile had to be adjusted accordingly, as visually represented in Fig. 6.4. To accommodate this, we redistributed the upper hole diameter limit of 450 nm to cover the missing phase fraction, highlighted in red. This adjustment clearly represents a fabrication compromise, and a substantially reduced efficiency is expected.

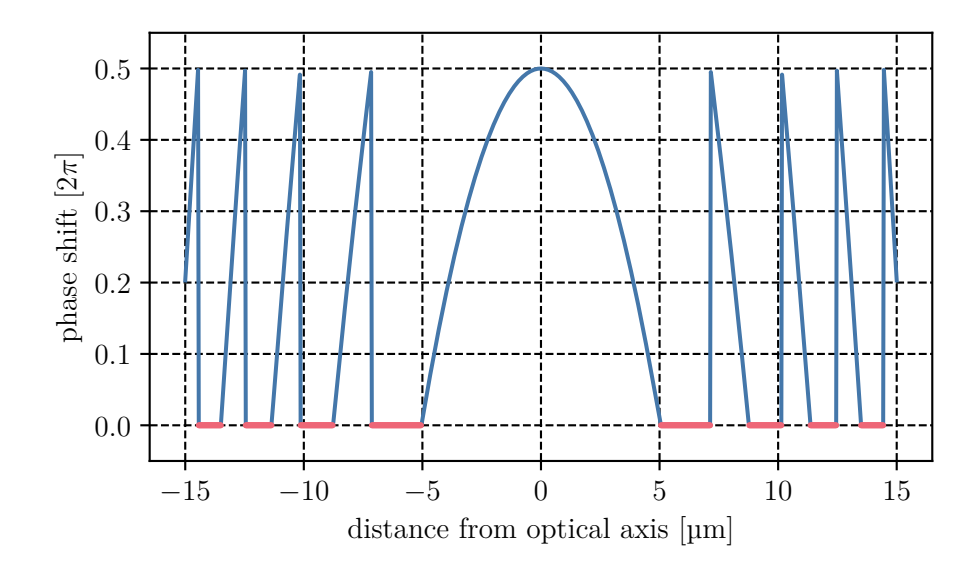


Figure 6.4: Visualization of the resist-only metalens phase map arising from the necessary fabrication compromises (highlighted in red).

Akin to the AlN full-lens FDTD simulations, we employed a cell size of 30x30x3 µm for the resist-only full-lens simulations. With a selected numerical aperture of 0.25, this resulted in a simulated lens with a focal length of 40 µm, illuminated by a Gaussian source with a diameter $(1/e^2)$ of 20 µm. The generated beam profile and its focal plane are depicted in Fig. 6.6. The plot demonstrates the intended function, with the focal spot positioned at the desired distance. It is noteworthy that a pronounced Poisson spot precedes the focal plane. As it is absent in the AlN beam profiles, it is likely induced by the constructive interference of the relatively large wavefronts that originate from the plateaus in the cropped phase map (Fig. 6.4).

We determined the spot size in the focal plane to be $w=2.3\,\mu\text{m}$. A diffraction-limited lens of the same numerical aperture generates a beam waist of $w_{d.l.}=1.6\,\mu\text{m}$. This implies a substantial enlargement of almost 50%, though it must be considered in light of the significantly limited phase coverage. A similar argument can be made about the efficiency of the metalens, which accumulates approximately 26.5% of the incident light in close proximity to the focal spot.

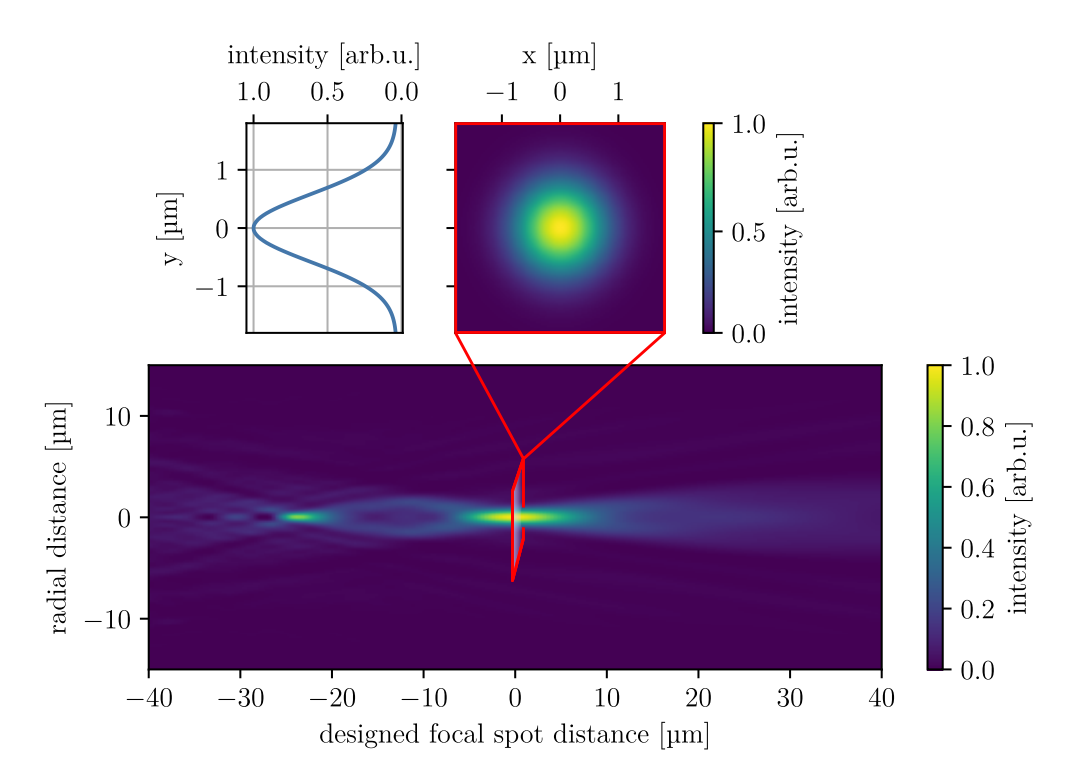


Figure 6.5: Simulated linear intensity profile of a resist-only metalens with a numerical aperture of 0.25.

Figure 6.6 presents the beam profile in a logarithmic scale. As anticipated due to the required design compromises, particularly the plateaus in the phase map, a significant portion of the incident intensity constructively interferes in front of the focal spot. Additionally, a fraction traverses the lens unaltered, resulting in the radial distribution of intensity.

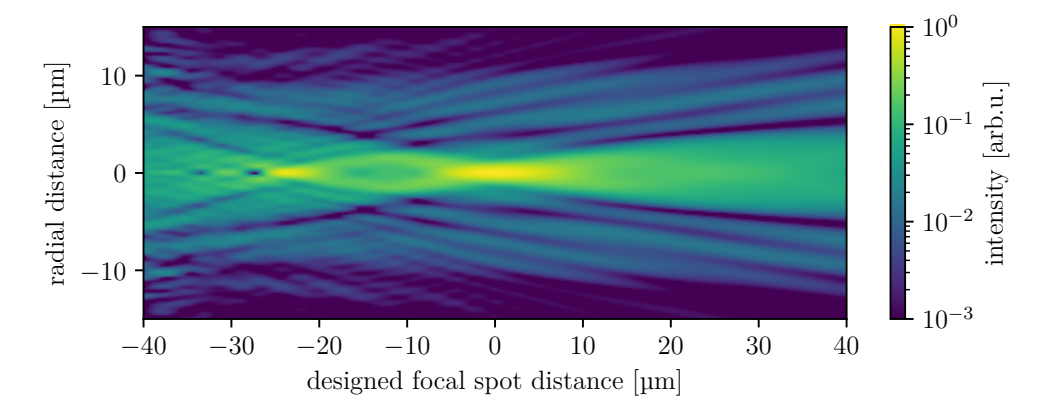


Figure 6.6: Simulated logarithmic intensity profile of a resist-only metalens with a numerical aperture of 0.25.

6.2 Fabrication

With the characterization process in mind, we chose a balance between size, fabrication time, and manageability, resulting in a lens diameter of 100 µm and a focal length of 500 µm. According to Eq. 4.2, this corresponds to a numerical aperture of 0.1. Regarding the involved process steps, the workflow aligns with that of the ALD templates and follows Fig. 5.4, including the same correction for proximity effects. However, as the new design involves dimensional changes, we conducted a new test series for the optimal dose. Figure 6.7 illustrates the results of this series, which range from apparent underexposure to severe overexposure. In particular, a dose bias toward the lower left quadrant, similar to that observed in Sect. 5.3.1, is again evident in the case of underexposure (Fig. 6.7, top left). Fortunately, for the interpolated ideal dose of approximately $49\,\mu\text{C/cm}^2$, the impact of this error is sufficiently reduced.

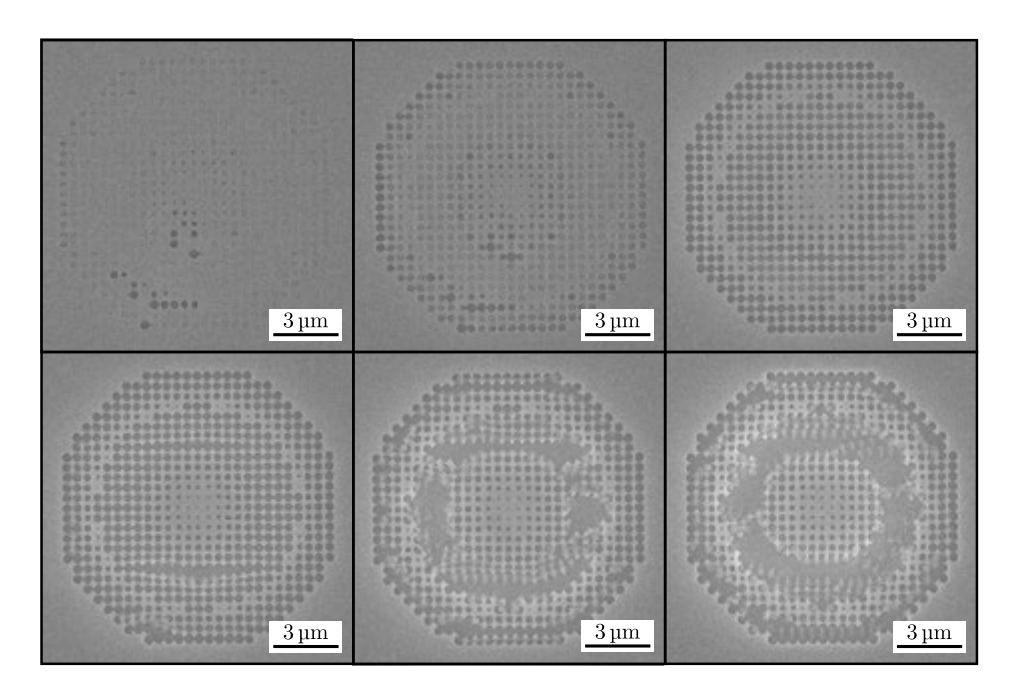


Figure 6.7: Test series on electron beam resist CSAR 62 across multiple exposure doses ranging from from 32.5 to $65\,\mu\text{C/cm}^2$ with an increment of $6.5\,\mu\text{C/cm}^2$.

Based on the ideal exposure dose, we patterned the resist-only metalens. Figure 6.8 illustrates a full view, along with several magnified images of the resulting lens. As evident from the superposition with the GDSII file, the structure closely matches the intended layout. Concerning the smallest (75 nm) and largest (450 nm) hole diameters, we observed maximum deviations of 15 nm. However, similar to the ALD templates, these deviations could be influenced by the destructive effect of imaging electrons.

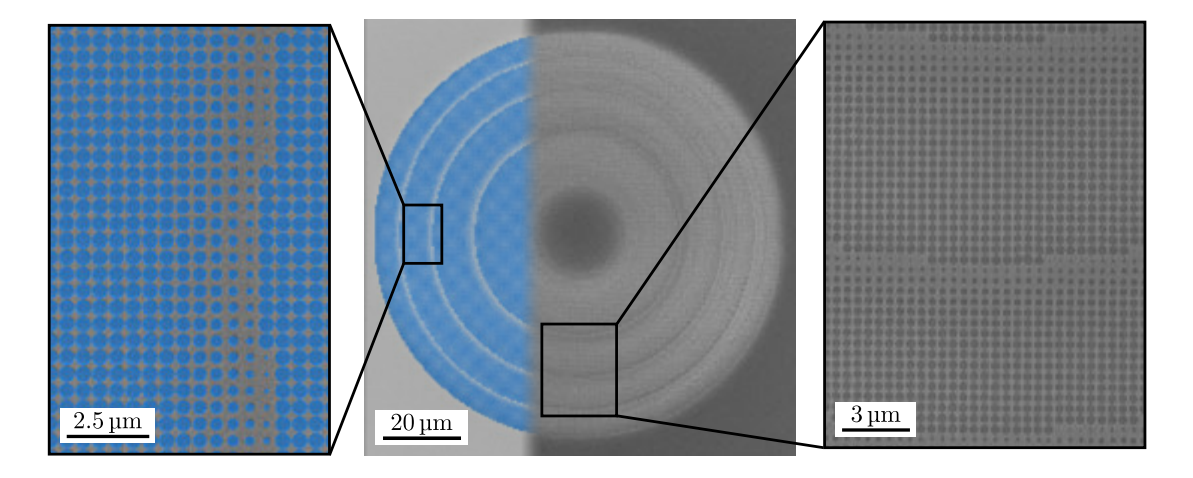


Figure 6.8: SEM images of fabricated resist-only metalens, superimposed with the targeted GDSII layout.

6.3 Characterization

To characterize the beam profile of the fabricated resist-only metalens, we built a custom experimental setup to image transverse slices along the propagation direction of the beam. Table 6.1 lists the components and Fig. 6.9 schematically depicts their positions within the setup.

Table 6.1: List of optical components used in the experimental setup of Fig. 6.9.

Component	Description	Specifications
Laser Source	CW HeNe laser	$\lambda = 633 \mathrm{nm}, P = 0.5 \mathrm{mW}$
Aperture	Adjustable diaphragm blades	
Metalens	Resist-only 0.1 NA lens	$f = 500 \mu \text{m}, D = 100 \mu \text{m}$
Imaging Lens	Bulk lens	$f = 100 \mathrm{mm}, D = 24.4 \mathrm{mm}$
Brightness control	Neutral-Density filter	
Detector	Photodiode detector	Pixel size: 3 μm ²

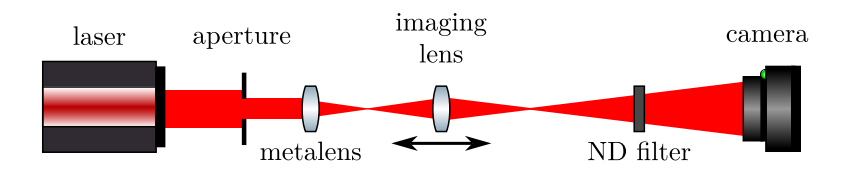


Figure 6.9: Schematic representation of the experimental setup used to characterize the beam profile of the resist-only metalens. Optical elements adapted from [41].

We positioned the imaging lens to maximize its magnification within the available space and thus utilize the resolution of the detector efficiently. With the metasurface at the object plane, this positioning achieved a magnification factor of approximately 6.62, corresponding to an imaging resolution of approximately 450 nm. Assuming the fully illuminated resist-only metalens to be diffraction-limited, Eq. 4.4 yields a hypothetical spot size of $w_{d,l} = 4.03 \,\mu\text{m}$, which is readily resolvable with this setup.

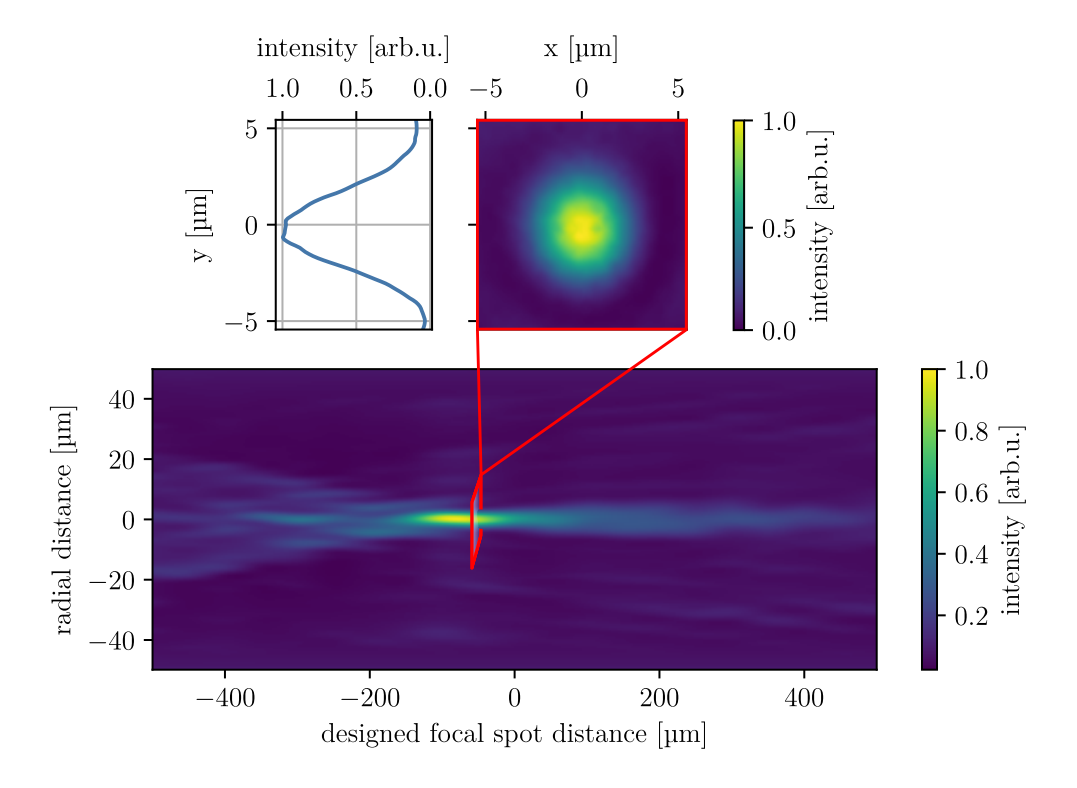


Figure 6.10: Intensity profile of the fabricated resist-only metalens with a numerical aperture of 0.1.

As indicated in Fig. 6.9, the imaging lens was mounted on a longitudinally adjustable stage. By increasing the distance between the meta- and imaging lens, we shifted the object plane away from the surface of the metalens. Accordingly, by careful adjustment of the stage's longitudinal position, the image formed in the camera plane can be scanned across the beam profile. Given that the focal length of the metalens is only $500 \, \mu m$, the effect of the shift on the magnification factor can be neglected.

Figure 6.10 illustrates the resulting beam profile for the 0.1 NA resist-only metalens, measured with this setup. The plot reveals that the focal plane of the lens is shifted by approximately 50 µm from the desired location. A comparable, albeit less pronounced deviation was observed in the simulation of the low-aperture AlN metalens, and is likely also attributable to the limited number of Fresnel zones within the lens's perimeter (Sect. 4.3.3). Upon closer inspection, the Poisson spot, which was rather pronounced in the simulation of the resist-only lens, is also discernable in Fig. 6.10. A measure-

ment of the minimum beam waist yielded a value of $w=7.1\,\mu\mathrm{m}$. In comparison to the diffraction-limited case, this implies an enlargement of approximately 75%. Approximately 19% of the incident intensity was accumulated within this diameter of the focal spot. Accordingly, the fabricated resist-only metalens demonstrates a performance which is only slightly lower than the (simulated) optimum. This proves the viability of the developed fabrication protocol.

7 Discussion and Conclusion

The objective of this thesis was to contribute to the advancement of metalens technology for the scientifically and industrially vital UV spectrum. To achieve this, we designed and optimized a functional UV metalens from the ground up. Given its exceptional refractive properties, including the highest UV refractive index of all eligible materials, the dielectric aluminum nitride (AlN) was singled out as optimal candidate for this investigation.

Propagation phase-based metalenses, as employed in this thesis, have, to our current knowledge, not yet been constructed using AlN. In fact, optimization of the metalens design by means of FDTD simulations demonstrated promising results. At a wavelength of 351 nm and numerical apertures of 0.1 and 0.5, we observed focusing efficiencies of 65% and 54%. Off-axis measurements based on the design of blazed gratings, at the corresponding half-opening angles of 5.7° and 26.6°, revealed beam redirection efficiencies of 61% and 42%. Table 7.1 provides an overview of the maximum achieved focusing efficiencies of comparable studies, elucidating the excellent performance of the present AlN metalens design. It should be noted that Tab. 7.1 refers specifically to metalens focusing efficiencies, thus providing the most accurate and comparable data to the present work.

Table 7.1: Overview of hitherto achieved maximum focusing efficiencies of manufacturable UV spectrum metalenses.

PP	Propagation	phase	GP	Geometric	nhase
ГГ	гторауалоп	DHase.	\TF	Стеонцевно	: ппаse

Reference	Material	Wavelength [nm]	Simulated efficiency [%]	Experimental efficiency [%]	Phase- modulation
[22]	HfO_{2}	364 266	-	55 56	PP PP
[42]	$\mathrm{Si}_{3}\mathrm{N}_{4}$	380	40	-	PP
[43]	AlN	375	47	-	GP
This work	AlN	351	54-65	-	PP

In light of the achieved theoretical performance of the AlN metalens design, we initiated preparatory work to realize a metalens. The selected fabrication strategy was atomic layer deposition (ALD), a previously untried yet promising fabrication approach for AlN metalenses. Based on electron beam lithography and the available positive resist CSAR 62, we fabricated high resolution ALD templates. In this process, rigorous optimization of the involved steps in conjunction with the correction of proximity effects achieved the required accuracy. Accordingly, templates with a diameter of $100 \, \mu m$, accumulating more than 10^6 elements with feature sizes down to 75 nm could be patterned

with a precision surpassing 15 nm.

To demonstrate that the achieved fidelity of these ALD templates provides an excellent foundation for all subsequent fabrication steps, we applied the same methodology to create a functional metalens from the template itself. Given the moderate refractive index of the resist (n=1.561) at the selected wavelength of $633\,\mathrm{nm}$, the design process of this resist-only metalens necessitated several compromises. Nonetheless, the realized devices achieved efficiencies of up to 27%. Despite being suboptimal due to design compromises, the capability of the resist-only metalens demonstrates the achieved fabrication fidelity, which should arguably suffice for the desired subsequent ALD process.

8 Future Perspectives

The promising computational results together with the established preparatory fabrication processes, provide an excellent foundation for the realization of AlN metalenses. Efforts are currently underway to identify a suitable collaboration that can provide the required ALD capabilities, which would then enable us to proceed with subsequent fabrication and characterization steps. Nevertheless, the results of this thesis demonstrate that AlN metalenses have the potential to establish new benchmarks in the near-UV regime. Furthermore, due to the wide bandgap of AlN (6 eV), its applicability extends beyond the investigated wavelength, potentially reaching far into the deep-UV spectrum. While AlN metalenses already hold promising potential, there remains room for improvement in enhancing the performance of the resist-only metalens:

- The insights gained from this study indicate that an increase in the FDTD simulation size could enhance the accuracy of low-aperture metalens simulations. While this approach would entail a greater computational cost, it would facilitate a more accurate comparison between the simulated and experimentally characterized metalens. Furthermore, this method would mitigate the aperture effects discussed in Sect. 4.3.3, particularly those observed in the blazed grating simulations.
- Diffraction induced by an unintended periodicity played a role, especially for the 26.6° blazed grating. One potential solution to this issue is the introduction of a variable unit cell, as suggested by Yu et al. [37].
- The suboptimal performance of the resist-only metalens could be substantially improved by an expansion of the phase coverage. The most straightforward approach would be an increased resist film thickness, either by multi-layer spin coating or a more viscous version of the resist. Regarding the former, in a separate collaboration on quarter-wave plate fabrication, we already demonstrated the reproducibility of double-layer coatings, which effectively doubled the resist film thickness.
- Although unproblematic for the fabricated 100 µm diameter metalenses, larger designs begin to show stress-induced cracks, as well as the collapse of free-standing structures due to capillary forces. In order to ensure the reliability of such projects, it is necessary to pay additional attention to the development process, including:
 - improvements to the adhesive strength of the electron beam resist. A possibility is the introduction of an adhesion promoter, obtainable by suppliers like Allresist GmbH [44].
 - mitigation of surface tension and thus prevention of capillary forces via critical point drying [45].

Bibliography

- [1] Richard P. Gallagher, Tim K. Lee, Chris D. Bajdik, and Marilyn Borugian. Ultraviolet radiation. *Chronic Diseases in Canada*, 29 Suppl 1:51–68, 2010.
- [2] Marcus Ossiander, Maryna Leonidivna Meretska, Hana Kristin Hampel, Soon Wei Daniel Lim, Nico Knefz, Thomas Jauk, Federico Capasso, and Martin Schultze. Extreme ultraviolet metalens by vacuum guiding. *Science*, 380(6640):59–63, April 2023.
- [3] Dong Zhao, Zhelin Lin, Wenqi Zhu, Henri J. Lezec, Ting Xu, Amit Agrawal, Cheng Zhang, and Kun Huang. Recent advances in ultraviolet nanophotonics: from plasmonics and metamaterials to metasurfaces. *Nanophotonics*, 10(9):2283–2308, July 2021.
- [4] F.H. Dill. Optical lithography. *IEEE Transactions on Electron Devices*, 22(7):440–444, July 1975.
- [5] Harun H. Solak. Nanolithography with coherent extreme ultraviolet light. *Journal of Physics D: Applied Physics*, 39(10):R171–R188, May 2006.
- [6] L.R. Harriott. Limits of lithography. Proceedings of the IEEE, 89(3):366-374, March 2001.
- [7] Jacques Lucas, Frederic Smektala, and Jean Luc Adam. Fluorine in optics. *Journal of Fluorine Chemistry*, 114(2):113–118, April 2002.
- [8] Winfried Kaiser. The Evolvement of Lithography Optics Towards Advanced EUV Lithography: Enabling the Continuation of Moore's Law for Six Decades. *IEEE Electron Devices Magazine*, 2(1):23–34, March 2024.
- [9] M. Schultze, A. Wirth, I. Grguras, M. Uiberacker, T. Uphues, A. J. Verhoef, J. Gagnon, M. Hofstetter, U. Kleineberg, E. Goulielmakis, and F. Krausz. Stateof-the-art attosecond metrology. *Journal of Electron Spectroscopy and Related Phe*nomena, 184(3):68-77, April 2011.
- [10] Jacob Engelberg and Uriel Levy. The advantages of metalenses over diffractive lenses. *Nature Communications*, 11(1):1991, April 2020.
- [11] Jie Hu, Sankhyabrata Bandyopadhyay, Yu-hui Liu, and Li-yang Shao. A Review on Metasurface: From Principle to Smart Metadevices. Frontiers in Physics, 8, January 2021.

- [12] Nanfang Yu, Patrice Genevet, Mikhail A. Kats, Francesco Aieta, Jean-Philippe Tetienne, Federico Capasso, and Zeno Gaburro. Light Propagation with Phase Discontinuities: Generalized Laws of Reflection and Refraction. *Science*, 334(6054):333–337, October 2011.
- [13] Meiyan Pan, Yifei Fu, Mengjie Zheng, Hao Chen, Yujia Zang, Huigao Duan, Qiang Li, Min Qiu, and Yueqiang Hu. Dielectric metalens for miniaturized imaging systems: progress and challenges. *Light: Science & Applications*, 11(1):195, June 2022.
- [14] Seong-Won Moon, Chihun Lee, Younghwan Yang, Joohoon Kim, Trevon Badloe, Chunghwan Jung, Gwanho Yoon, and Junsuk Rho. Tutorial on metalenses for advanced flat optics: Design, fabrication, and critical considerations. *Journal of Applied Physics*, 131(9):091101, March 2022.
- [15] Mohammadreza Khorasaninejad and Federico Capasso. Broadband Multifunctional Efficient Meta-Gratings Based on Dielectric Waveguide Phase Shifters. Nano Letters, 15(10):6709–6715, October 2015.
- [16] M. Khorasaninejad, A. Y. Zhu, C. Roques-Carmes, W. T. Chen, J. Oh, I. Mishra, R. C. Devlin, and F. Capasso. Polarization-Insensitive Metalenses at Visible Wavelengths. *Nano Letters*, 16(11):7229–7234, November 2016.
- [17] Philippe Lalanne and Pierre Chavel. Metalenses at visible wavelengths: past, present, perspectives. Laser & Photonics Reviews, 11(3):1600295, 2017.
- [18] Christopher Palmer and Erwin G Loewen. *Diffraction grating handbook*. Newport Corporation New York, 2005.
- [19] Amir Arbabi, Ehsan Arbabi, Mahdad Mansouree, Seunghoon Han, Seyedeh Mahsa Kamali, Yu Horie, and Andrei Faraon. Increasing efficiency of high numerical aperture metasurfaces using the grating averaging technique. *Scientific Reports*, 10(1):7124, April 2020.
- [20] Shang Sun, Zhenxing Zhou, Chen Zhang, Yisheng Gao, Zonghui Duan, Shumin Xiao, and Qinghai Song. All-Dielectric Full-Color Printing with TiO2 Metasurfaces. ACS Nano, 11(5):4445–4452, May 2017.
- [21] Sergei V. Zhukovsky, Andrei Andryieuski, Osamu Takayama, Evgeniy Shkondin, Radu Malureanu, Flemming Jensen, and Andrei V. Lavrinenko. Experimental Demonstration of Effective Medium Approximation Breakdown in Deeply Subwavelength All-Dielectric Multilayers. *Physical Review Letters*, 115(17):177402, October 2015.
- [22] Cheng Zhang, Shawn Divitt, Qingbin Fan, Wenqi Zhu, Amit Agrawal, Yanqing Lu, Ting Xu, and Henri J. Lezec. Low-loss metasurface optics down to the deep ultraviolet region. *Light: Science & Applications*, 9(1):55, April 2020.

- [23] Taewook Nam, Hyunho Lee, Taejin Choi, Seunggi Seo, Chang Mo Yoon, Yunjung Choi, Heonjong Jeong, Hima K. Lingam, Venkateswara R. Chitturi, Andrey Korolev, Jong-Hyun Ahn, and Hyungjun Kim. Low-temperature, high-growth-rate ALD of SiO2 using aminodisilane precursor. Applied Surface Science, 485:381–390, August 2019.
- [24] Taiyu Okatani, Yuya Naito, and Yoshiaki Kanamori. Fabrication of high-aspectratio SiO ₂ nanopillars by Si thermal oxidation for metalenses in the visible region. Japanese Journal of Applied Physics, 62(SG):SG1034, June 2023.
- [25] P. Motamedi and K. Cadien. Structural and optical characterization of low-temperature ALD crystalline AlN. Journal of Crystal Growth, 421:45–52, July 2015.
- [26] Joohoon Kim, Dongmin Jeon, Junhwa Seong, Trevon Badloe, Nara Jeon, Gyeongtae Kim, Jaekyung Kim, Sangwon Baek, Jong-Lam Lee, and Junsuk Rho. Photonic Encryption Platform via Dual-Band Vectorial Metaholograms in the Ultraviolet and Visible. ACS Nano, 16(3):3546–3553, March 2022.
- [27] Il Hoon Lee, Tea Young Lee, Su Min Hwang, and Chee Won Chung. Etch characteristics of MgO thin films in Cl2/Ar, CH3OH/Ar and CH4/Ar plasmas. *Vacuum*, 101:394–398, March 2014.
- [28] Joohoon Kim, Wonjoong Kim, Dong Kyo Oh, Hyunjung Kang, Hongyoon Kim, Trevon Badloe, Seokwoo Kim, Chanwoong Park, Hojung Choi, Heon Lee, and Junsuk Rho. One-step printable platform for high-efficiency metasurfaces down to the deep-ultraviolet region. *Light: Science & Applications*, 12(1):68, March 2023.
- [29] Joon-Suh Park, Soon Wei Daniel Lim, Arman Amirzhan, Hyukmo Kang, Karlene Karrfalt, Daewook Kim, Joel Leger, Augustine Urbas, Marcus Ossiander, Zhaoyi Li, and Federico Capasso. All-Glass 100 mm Diameter Visible Metalens for Imaging the Cosmos. ACS Nano, 18(4):3187–3198, January 2024.
- [30] Luis V. Rodríguez-de Marcos, Juan I. Larruquert, José A. Méndez, and José A. Aznárez. Self-consistent optical constants of SiO₂ and Ta₂O₅ films. *Optical Materials Express*, 6(11):3622–3637, November 2016.
- [31] Leonid Yu. Beliaev, Evgeniy Shkondin, Andrei V. Lavrinenko, and Osamu Takayama. Thickness-dependent optical properties of aluminum nitride films for mid-infrared wavelengths. *Journal of Vacuum Science & Technology A*, 39(4):043408, May 2021.
- [32] M. F. Al-Kuhaili. Optical properties of hafnium oxide thin films and their application in energy-efficient windows. *Optical Materials*, 27(3):383–387, December 2004.
- [33] Herbert R. Philipp. Optical Properties of Silicon Nitride. *Journal of The Electro*chemical Society, 120(2):295, February 1973.

- [34] S. B. Ippolito, B. B. Goldberg, and M. S. Ünlü. Theoretical analysis of numerical aperture increasing lens microscopy. *Journal of Applied Physics*, 97(5):053105, February 2005.
- [35] David S. Simon. A Guided Tour of Light Beams: From lasers to optical knots. Morgan & Claypool Publishers, November 2016.
- [36] International Organization for Standardization. ISO 11146-1:2021(en) Lasers and laser-related equipment Test methods for laser beam widths, divergence angles and beam propagation ratios, 2021.
- [37] Chen-Yi Yu, Yen-Chun Chen, Qiu-Chun Zeng, Wei-Lun Hsu, and Chih-Ming Wang. Optical performance of synthetic aperture metalens based on hybrid unit-cells. *Materials Science in Semiconductor Processing*, 170:107982, February 2024.
- [38] Robert C. Devlin, Mohammadreza Khorasaninejad, Wei Ting Chen, Jaewon Oh, and Federico Capasso. Broadband high-efficiency dielectric metasurfaces for the visible spectrum. Proceedings of the National Academy of Sciences, 113(38):10473–10478, September 2016.
- [39] Gemma Rius Suñé. Electron beam lithography for Nanofabrication. Ph.D. Thesis, Universitat Autònoma de Barcelona, March 2008.
- [40] Allresist GmbH. Data Sheet for E-Beam Resist AR-P 6200 series (CSAR 62). Technical report, 2022.
- [41] Alexander Franzen. ComponentLibrary: a free vector graphics library for optics, 2024
- [42] Saima Kanwal, Jing Wen, Binbin Yu, Xu Chen, Dileep Kumar, Yi Kang, Chunyan Bai, Saima Ubaid, and Dawei Zhang. Polarization Insensitive, Broadband, Near Diffraction-Limited Metalens in Ultraviolet Region. *Nanomaterials*, 10(8):1439, August 2020.
- [43] Linhao Guo, Zelin Hu, Rongqiao Wan, Linyun Long, Tao Li, Jianchang Yan, Yun Lin, Lei Zhang, Wenhui Zhu, and Liancheng Wang. Design of aluminum nitride metalens for broadband ultraviolet incidence routing. *Nanophotonics*, 8(1):171–180, January 2019.
- [44] Allresist GmbH. Data Sheet for Adhesion Promoter AR 300-80. Technical report, 2024.
- [45] J. L. Pearson and D. R. S. Cumming. A single-step process for making nanofluidic channels using electron beam lithography. *Microelectronic Engineering*, 78-79:343– 348, March 2005.
- [46] Kane Yee. Numerical solution of initial boundary value problems involving maxwell's equations in isotropic media. *IEEE Transactions on Antennas and Propagation*, 14(3):302–307, May 1966.

[47] John B. Schneider. Understanding the FDTD Method. Washington State University, 2010.

Appendix

Finite-Difference Time-Domain Simulations

Developed in the late 1960s by Kane S. Yee [46], finite-difference time-domain (FDTD) is a widely used numerical technique for solving Maxwell's equations. Actuated by its broad applicability in fields like optics and nanophotonics, it has become a fundamental tool in computational electromagnetics. While the method is generally perceived as computationally expensive, this challenge is mitigated by its ease of parallelization, which allows for an efficient distribution across multiple processing units. In the scope of full-wave techniques, FDTD is specifically well suited to dealing with problems that feature characteristic dimensions coinciding in size with the wavelength(s) of interest.

As the name suggests, FDTD exploits the finite-difference method (Eq. 8.1) to solve the temporal and spatial derivatives appearing in Maxwell's equations. The approximation is based on the Taylor expansion of a function f(x) around $x \pm \frac{\delta}{2}$.

$$\frac{df(x)}{dx}\bigg|_{x=x_0} = \frac{f(x_0 + \frac{\delta}{2}) - f(x_0 - \frac{\delta}{2})}{\delta} + O(\delta^2) \approx \frac{f(x_0 + \frac{\delta}{2}) - f(x_0 - \frac{\delta}{2})}{\delta}$$
(8.1)

The implementation of the Yee algorithm will, for simplicity's sake, be outlined in 1D, based on the work in [47]. The underlying concept is substantially upheld in higher dimensions. In the present example, the wave is linearly polarized along the z-axis and propagates along the x-axis. Equation 8.2 and 8.3 show the scalar relation entailed by these 1D restrictions.

$$-\mu \frac{\partial \mathbf{H}}{\partial t} = \mathbf{\nabla} \times \mathbf{E} = -\hat{e}_y \frac{\partial E_z}{\partial x} \implies \mu \frac{\partial H_y}{\partial t} = \frac{\partial E_z}{\partial x}$$
(8.2)

$$\epsilon \frac{\partial \mathbf{E}}{\partial t} = \mathbf{\nabla} \times \mathbf{H} = \hat{e}_z \frac{\partial H_y}{\partial x} \quad \Rightarrow \quad \epsilon \frac{\partial E_z}{\partial t} = \frac{\partial H_y}{\partial x}$$
(8.3)

For a concise derivation of the finite distances, the notation delineated in Eq. 8.4 and 8.5 shall be employed henceforth. Therein Δ_t and Δ_x denote the temporal and spatial periodicity with q and m representing their respective indices.

$$E_z(x,t) = E_z(m\Delta_x, q\Delta_t) = E_z^q[m]$$
(8.4)

$$H_y(x,t) = H_y(m\Delta_x, q\Delta_t) = H_y^q[m]$$
(8.5)

The actual discretization is implemented by the so-called Yee-grid. It places the electric and magnetic fields at staggered positions in space and time, essentially extending the initial 1D problem into two dimensions. Based on this grid the derivatives in Eq. 8.2

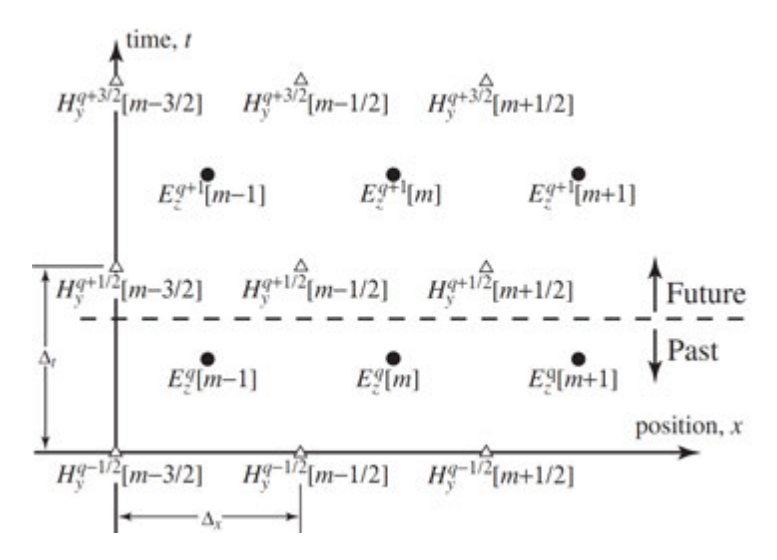


Figure 8.1: Schematic representation of a Yee-grid for a one dimensional problem. Nodes of the electric and magnetic field are indicated with circles and triangles, respectively. Adapted from [47].

and 8.3 are translated into Eq. 8.6 and 8.7. A schematic arrangement reflecting this discretization is depicted in Fig. 8.1.

$$\mu \frac{H_y^{q+\frac{1}{2}} \left[m + \frac{1}{2} \right] - H_y^{q-\frac{1}{2}} \left[m + \frac{1}{2} \right]}{\Delta_t} = \frac{E_z^q [m+1] - E_z^q [m]}{\Delta_x}$$
(8.6)

$$\epsilon \frac{E_z^{q+1}[m] - E_z^q[m]}{\Delta_t} = \frac{H_y^{q+\frac{1}{2}} \left[m + \frac{1}{2} \right] - H_y^{q+\frac{1}{2}} \left[m - \frac{1}{2} \right]}{\Delta_x}$$
(8.7)

The finite differences are now molded into update equations by solving for the temporally advancing term. Correlating Eq. 8.8 and 8.9 with figure 8.1, it is apparent that the terms describing the progression of the field solely depend on previous (known) terms. Accordingly, the dashed line indicated in the schematic grid temporally advances with each evaluation of Eq. 8.8 and 8.9. This concept of jumping back and forth between the fields to progress in time is referred to as the leap-frog method.

$$H_y^{q+\frac{1}{2}}\left[m+\frac{1}{2}\right] = H_y^{q-\frac{1}{2}}\left[m+\frac{1}{2}\right] + \frac{\Delta_t}{\mu\Delta_x}\left(E_z^q[m+1] - E_z^q[m]\right)$$
(8.8)

$$E_z^{q+1}[m] = E_z^q[m] + \frac{\Delta_t}{\epsilon \Delta_x} \left(H_y^{q+\frac{1}{2}} \left[m + \frac{1}{2} \right] - H_y^{q+\frac{1}{2}} \left[m - \frac{1}{2} \right] \right)$$
(8.9)

Finally, the stability condition of the algorithm is given by Eq. 8.10. As in dealing with electromagnetic waves, the maximum speed at which information can travel is the speed of light in free space c. It, therefore, comes naturally that to ensure convergence, the discretization in the spatial grid cannot surpass the factor $c\Delta_t$. Following this restriction, the so-called Courant factor S must be smaller than unity. In the case

of higher dimensions it is important to note that Eq. 8.10 must be multiplied by an additional factor of $1/\sqrt{d}$, where d corresponds to the dimensionality.

$$S = \frac{c\Delta_t}{\Delta_x} \le 1 \tag{8.10}$$